ORIGINAL RESEARCH

Investigating and evaluating the seismic behavior of the proposed connection in the moment resistance steel frame

Mehri Asgari[1], Mohammad Reza Adib Ramezani[2]*

Abstract:

In this study, the pre-approved connection and the proposed connection have been investigated and analyzed using Abaqus finite element software. Non-linear static analysis was performed with reciprocating loading. In this study, in order to compare the proposed connection and the direct connection, two one-story and six-story frames has been modeled and the behavior of the two connections in these frames has been investigated. According to the software models, it can be seen that in all the models, the bending moment capacity of the connection is more than 40% of the calculated plastic moment in the connection. In connection with the reduced cross-section, this percentage has reached nearly 20%. The results of the proposed connection behavior show an improvement of approximately 25-34% compared to the pre-qualified connections in accordance with the American Institute of Steel Construction (AISC) standards. The structure with the proposed connection has a higher coefficient of behavior than direct connection. With the increase in the height of the structure, the coefficient of behavior of the structure has also decreased.

1. Introduction

Connections have been one of the most important concerns of structural science scientists in recent decades. Paying more attention to the beam-to-column load transfer path and making sure that this load transfer path is safe at the ultimate limit of the behavior of the lateral load-carrying system is one of the major differences in recent approaches.
The first written functional study of concrete beam-to-column connection was done by Hansen and Conner at the Portland Cement Association (PCA) laboratory [1]. Since then, this issue has been studied by researchers in many countries. Although the goals of these researches were different, the main emphasis of these studies was to examine the connection behavior and create deformable behavior in cyclic loading [2]. The result of this research led to the drafting of the first regulations for the design of reinforced concrete joints. ASCE-ACI Committee 352 published the first design recommendations in 1976. At the same time, several recommendations were developed by different statutes, but these recommendations and laws had differences with each other in practice. In the following years, more research by researchers [4-3] led to the amendment of the ASCE-ACI-352 committee's recommendation, which in 2002, 1991 and 1985, new editions were published [5-6 and 2]. In recent years, with the development of the use of high-strength

concrete, fiber concrete and self-compacting concrete, research in this field has focused on investigating the performance of joints made with the above materials [7 and 10]. An experimental and numerical study related to the cross-section of reduced IPE beams using box stiffeners was done by Roudsari et al [11]. Considering the reduction of beam width in RBS section potentially increases the possibility of lateral buckling connection, the idea of box stiffeners was proposed to overcome this deficiency. The results showed that the stiffeners significantly increase the ductility of the joint without changing its strength. Montuori and Sagarese [12] used RBS steel to increase the ductility of wooden structures. They proposed a set of criteria to guarantee the creation of a plastic joint. Finally, a design diagram was presented that can be used for similar connections.

In 2019, Wang et al. [13] investigated the behavior of a steel beam connected to a column with an end plate. The test results showed that the plates in the joints can effectively move the plastic joint on the beam away from the column and reduce the force.

In 2019, Ahmadi et al. [14] conducted a laboratory investigation of the bending connection with stiffener. The proposed connection has very high resistance, stiffness and ductility and is classified as a resistant and stiff connection.

In another study conducted by Atmaji et al. [15] in 2019, on the steel connection model, based on the results of the modeling that has been done, it has satisfied the connection modeling that has sufficient ductility.

Other researchers have conducted research on the rules of the European regulation [16]. Jamshidi et al. [17] in 2020, to control the elastic behavior of columns, the use of columns with steel box-shaped sections filled with concrete as boundary elements and ring-shaped panels as webs is suggested. In order to control the elastic behavior of the column, the outstretching of the wing adjacent to the filler sheet has been investigated. It can be seen that the use of ring-shaped sheets has a significant effect in reducing the outward elongation of the column wing. In other words, the use of ringed sheets can prevent vertical boundary elements from yielding.

Ghalenoi et al [18] have conducted a research in 2019. The present research has studied the behavior of steel columns under compressive load with eccentricity with a laboratory approach. The results show that samples filled with fiber concrete have more energy absorption than concrete samples filled with simple concrete.

In 2017, Hijazi et al [19] conducted a study on the performance parameters of welded joints under cyclic loading. In this research, the behavior of the connection plates in the convergent bracing steel frame has been investigated using double profile braces and connecting pieces. Investigations showed that removing the free line of bending greatly increases the values of the plastic strains of the plate-bracket weld and the plastic strains of the plate connection. The highest amount of energy loss in the sample with stiffener was at the edge of the sheet, which increased by 15.4% compared to the sample without stiffener.

In the work of Hejazi et al. [20] in 2014, by using numerical modeling by nonlinear finite element method in the ABAQUS software environment, the behavior of composite columns including steel pipes filled with concrete under lateral loading and axial compressive load was studied. According to the results obtained in short columns in unrestricted contact mode, the composite column has more axial load capacity. Based on the analysis results of group (b) models, with the increase in column length, their lateral load capacity decreases drastically.

2- Numerical modeling with Abaqus software

In this section, modeling of connections in Abaqus software is discussed. The specifications entered in the software are as follows. In this research, the uniaxial behavior of steel was simulated by the classical plasticity model of metals in Abaqus software. In this model, the behavior of the steel is assumed to be completely elastic-plastic and the yield surface is von mises, and

the tensile and compressive strength of the steel is assumed to be the same. Figure 1 shows the stress-strain diagram of steel.
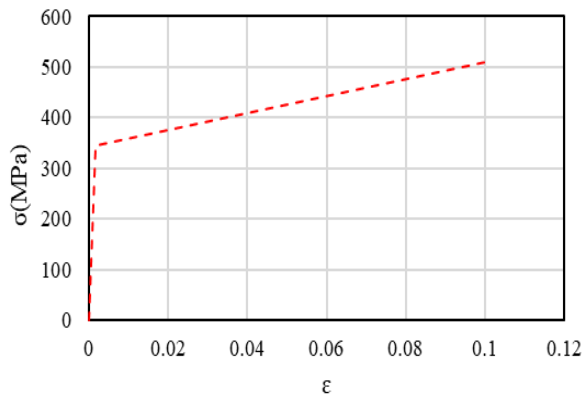

Figure 1- Stress-strain curve of steel longitudinal reinforcements (stress in MPa)

According to Figure 1, after the yield point, the slope of the second segment of the stress-strain curve reduces to 10% of the elastic modulus (E). This reduced slope represents the strain-hardening behavior of ST37 steel in the plastic region, where the material's stiffness decreases to 10% of its original value in the elastic range. For the steel model, the properties of Ductile Damage have been used. Table 1 presents these values.

Table 1- Ductile Damage specifications for steel

A	B	c	c_1	c_2	d_1	d_2	d_3
1.96	0.0001	2.86	1.24	2.913	1.23	1.405	-0.303

Each parameter in Table 1, which specifies ductile damage for steel used in Abaqus, is explained below:

1. d3: This parameter typically represents the damage parameter associated with the plastic deformation of the material. It can reflect the onset of ductile damage and is critical for defining the transition from elastic to plastic behavior.

2. d2: This parameter usually indicates the critical damage level at which significant plastic deformation occurs. It helps define the ductile behavior of the material and can influence the material's response under loading.
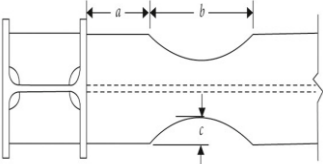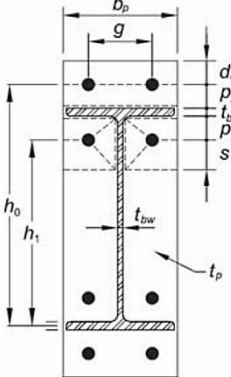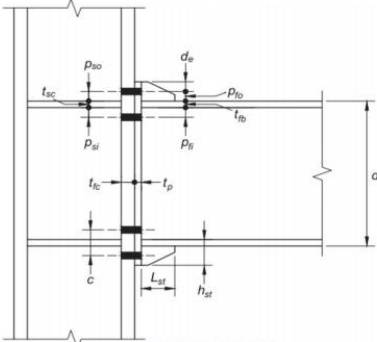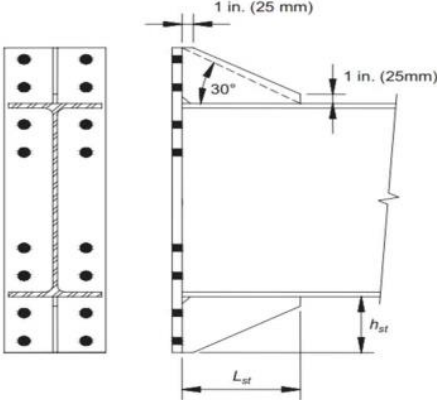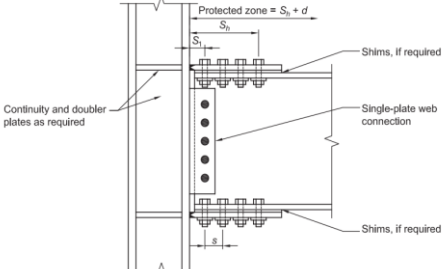
3. d1: Often referred to as the initial damage parameter, it represents the damage accumulation threshold at the onset of yielding. This parameter is essential for establishing the point at which the material begins to exhibit significant plastic deformation.

4. c2: This parameter is related to the energy absorbed by the material during loading. It may represent the threshold energy required for the initiation of damage or the energy dissipated during plastic deformation.

5. c1: Similar to c2, this parameter indicates the energy associated with the damage process but may relate to a different stage or aspect of the energy dissipation mechanism.

6. c: This parameter is often a scalar value that can influence the damage evolution law. It may be used to adjust the sensitivity of the damage model to loading conditions.

7. B: This parameter typically refers to a material constant that can affect the rate of damage accumulation. It plays a significant role in defining how quickly the material reaches the damage threshold under applied loads.

8. A: This parameter is generally a scaling factor that influences the overall damage evolution behavior. It can affect the material's ductility and how damage evolves under cyclic loading conditions.

These parameters are essential for accurately modeling ductile damage behavior in steel

within Abaqus, helping predict how the material will perform under various loading conditions. Table 2, all models examined, as illustrated.

Table 2- The models examined in this research

Model	Figure	Parts	Name
Reduced beam section		a=150 mm, b=320 mm, and c=40 mm.	RBS
bolted unstiffened extended end-plate		*Plate* $600 \times 200 \times 30mm$	BUEEP
Bolted stiffened extended end plate (4 screws)		*Plate* $600 \times 200 \times 30mm$ *Stiffner* $440 \times 180mm$	BSEEP
Bolted stiffened extended end plate (8 screws)		*Plate* $800 \times 350 \times 30mm$ *Stiffner* $400 \times 150mm$	BSEEP
Bolted flange plate		*Plate* $250 \times 300 \times 30mm$ *Plate* $300 \times 300 \times 25mm$	BFP

The proposed connection			
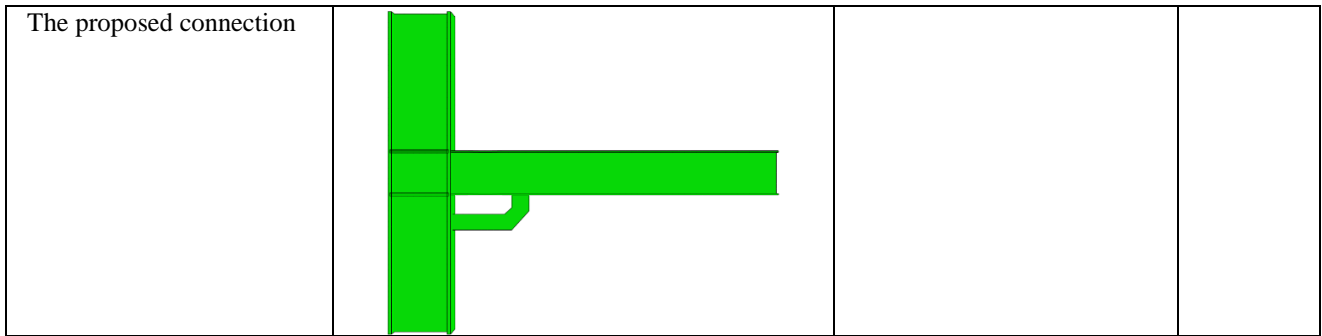
Eight-node cubic elements were used for concrete modeling, and Solid elements were used for beams, columns and stiffeners. Also, the modeled geometry has been partitioned using the partition command for regular meshing. The modeled geometry of the sample in the software is shown in figure (2). In Figure 3, the RBS section connection and protected zone are illustrated, while Figure 4 depicts the proposed connection.
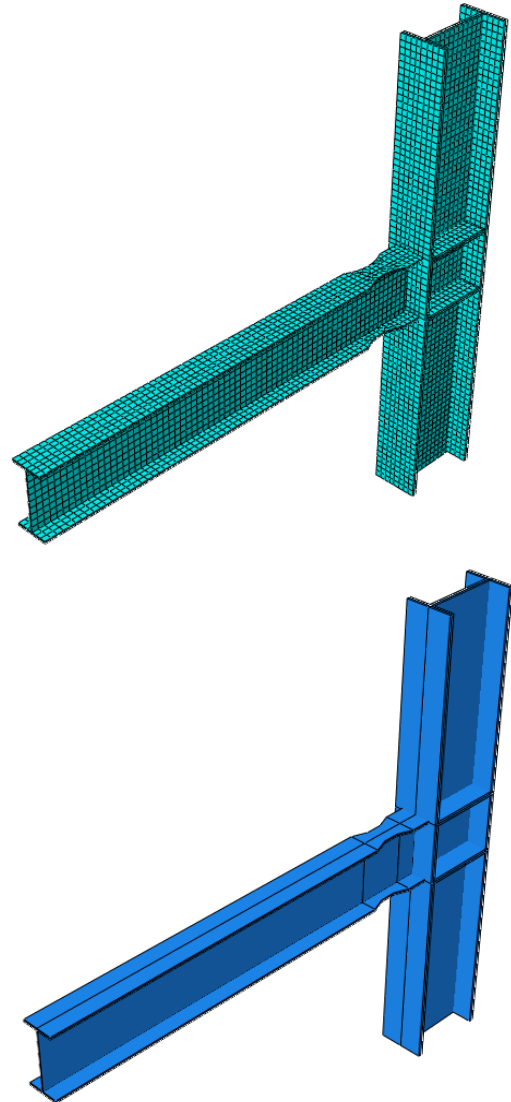

Figure 2- The partition created on the beam and column to perform a regular mesh on the model
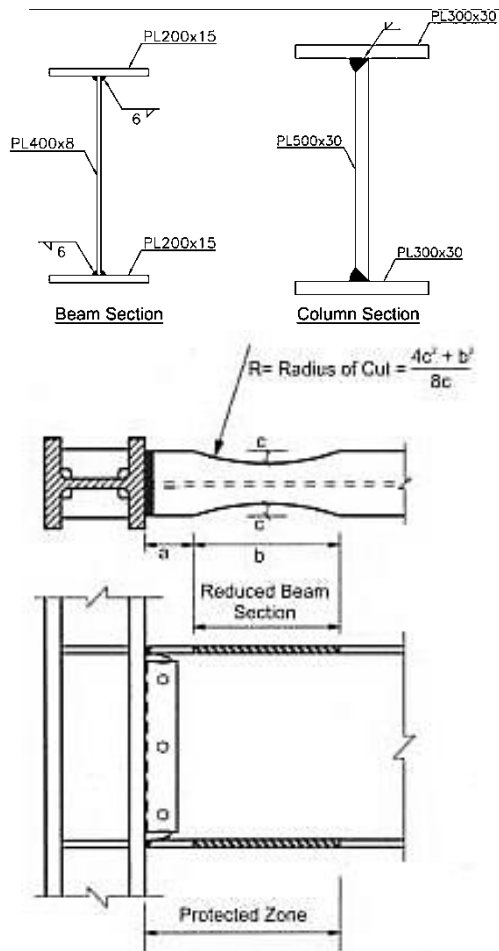
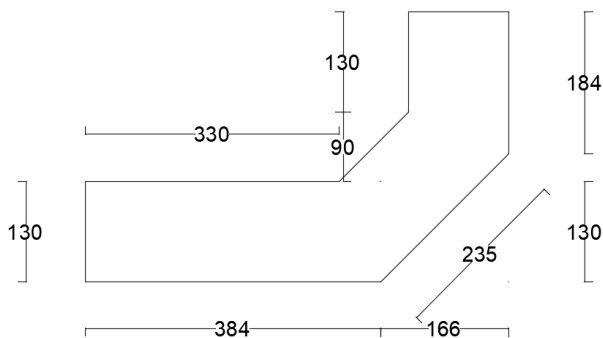**Figure 3- RBS section connection and protected zone**

Figure 4- proposed connection

This direct beam connection is reduced in cross-section. The beam dimensions are 400x8 mm in the web part and 200x15 mm in the wing part. The column also has a web with 500x30 mm sheet and 300x30 mm wings. The reduced part has the following dimensions: a=15 cm, b=32 cm, and c=4 cm.

For the regular mesh model of C3D8R type, i.e., a regular cubic three-dimensional element with 8 nodes is selected for integration and integration of the reduced type. In the validation model, the mesh convergence test has been performed on the model. In the verification model, the optimal mesh after several stages of analysis was a mesh with dimensions of 1 cm.

The boundary conditions of the laboratory sample were such that the displacement of all the nodes located at the top and bottom of the column were restricted in a joint manner. It is also tied in the middle part for out-of-plane buckling. All border and support conditions have been applied in the modeling. Cyclic loading has been applied to the model as in Figure 5. This loading has been selected based on the validation article model and according to the regulation of China [11], This loading was applied until the failure of the model.
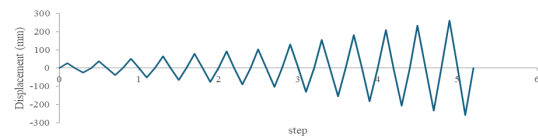

Figure 5- Load diagram applied to the model

Boundary conditions are also closed at the top and bottom of the displacement column, so-called joint supports are used, and the loading is applied as a displacement in accordance with Figure 5 at the end of the beam. The displacement load is given as a cyclic protocol at the end of the beam. The interaction between parts is selected from the surface-to-surface interaction type, and also in the screw connection from the surface-to-node connection type. The contact behavior between the surfaces of the normal type and the hard object is chosen so that the two objects are not placed inside each other during the analysis, and the coefficient of 0.3 is used for the friction surfaces between the two surfaces. For the screw modeling, pre-stressing force is determined based on the tenth topic of the national regulation, and its element is also selected as a solid type and is like the beam and column element.
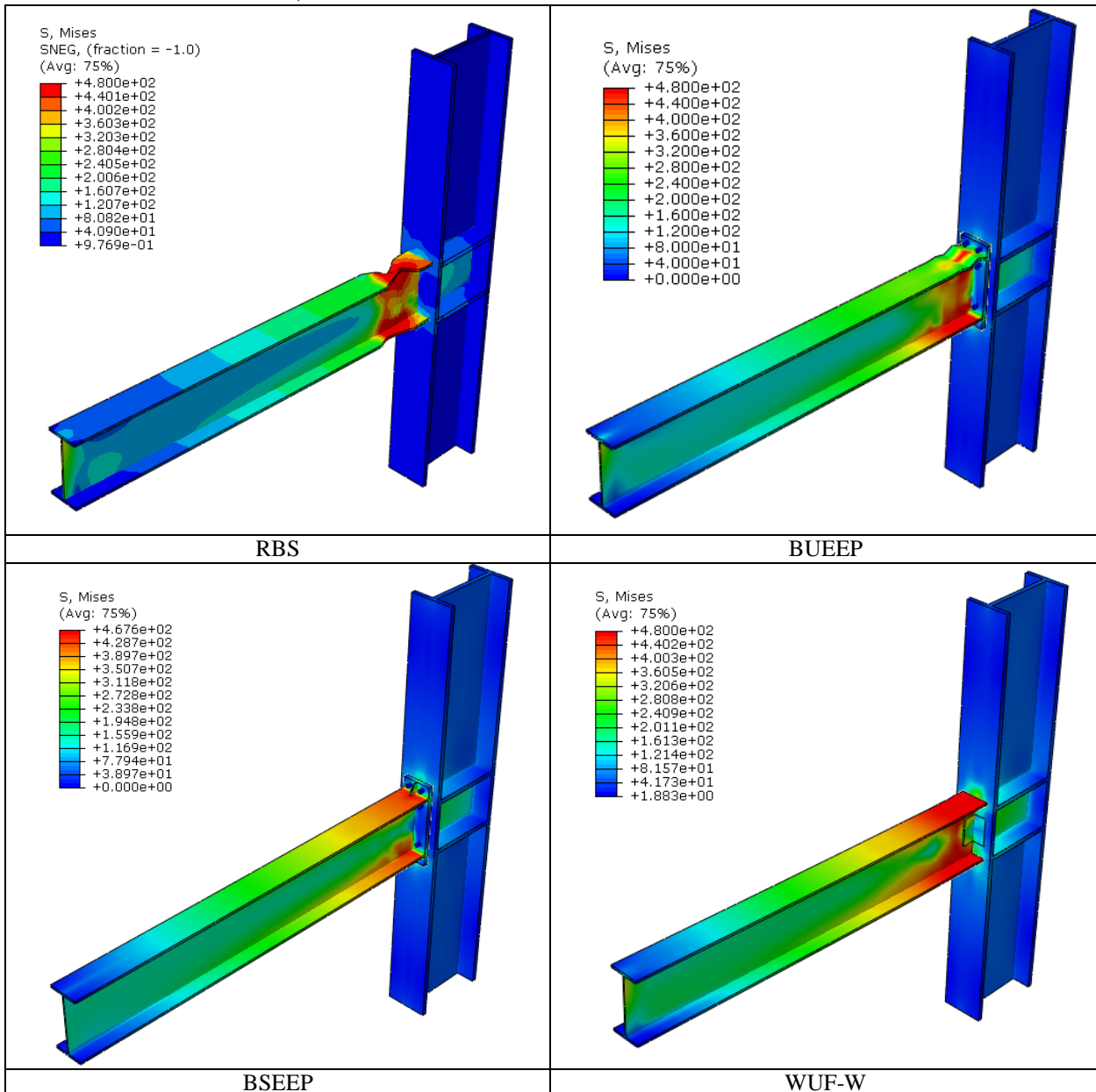
In this part, it is applied in the form of history and in a step-by-step manner, therefore, static analysis has been used. We have considered the time of the analysis to be equal to the duration of the steps. It should be noted that

the stress unit for the models in this section is based on N/m^2.

3- The results of the analysis on the models

The results are divided into two categories, graphical results and numerical results, and to check the graphical results, the von Mises stress and equivalent plastic strain are checked and evaluated, and to check the numerical results, the hysteresis chart will be evaluated. In the following, the graphical results of stress and equivalent plastic strain will be evaluated for the examined connection model. In Figure 4, the stress of the examined connections is displayed. The von Mises stress was observed at the moment of maximum displacement in the structure (Figure 6).

RBS	BUEEP
BSEEP	WUF-W

The proposed connection of the first model	The proposed connection of the second model
The proposed connection of the third model	The proposed connection of the fourth model
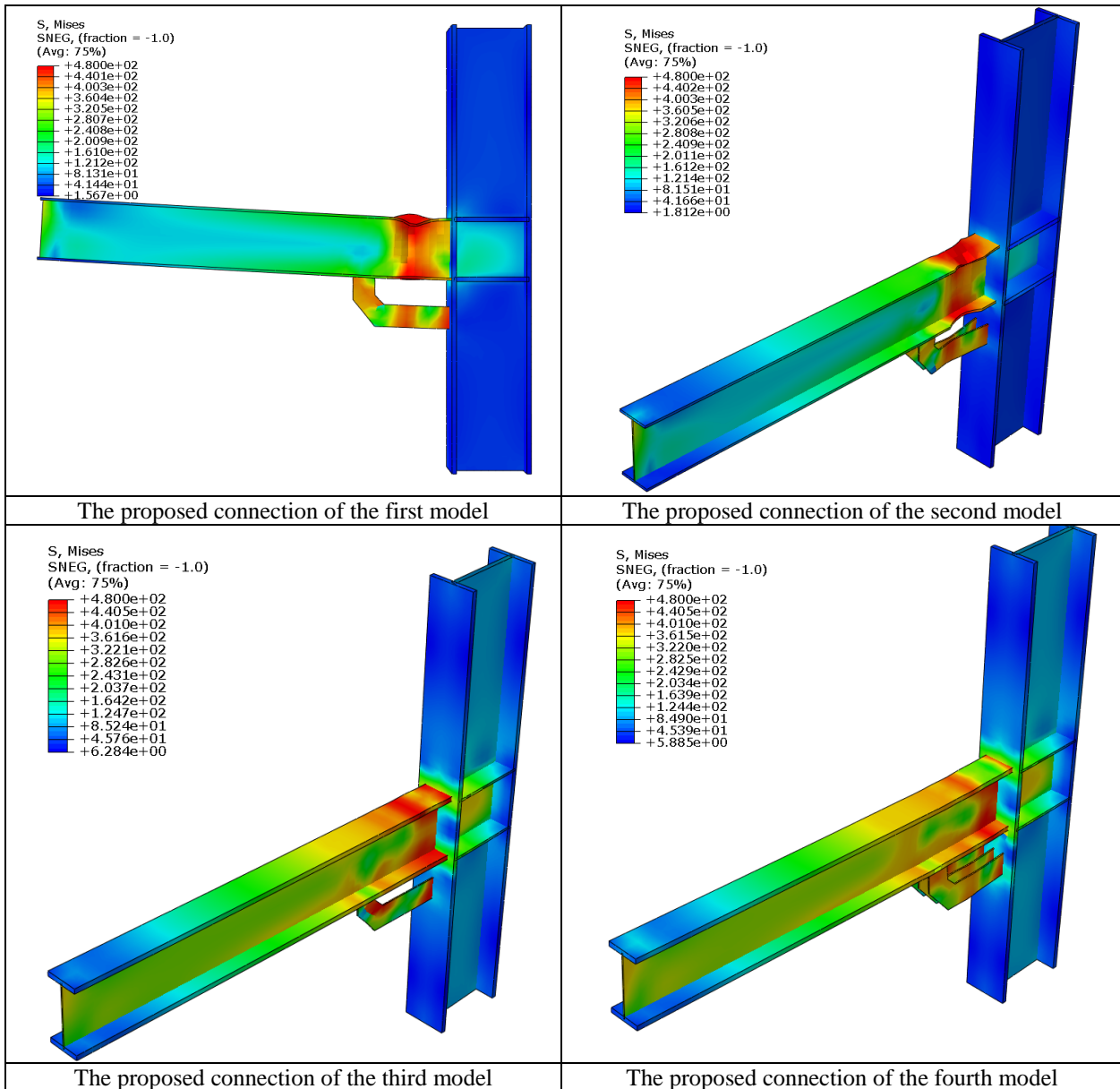
Figure 6- Von Mises stress in the examined joints (stress unit N/mm²)

Figure 7 shows the equivalent plastic strain for the considered connections.

RBS	BUEEP

BSEEP	WUF-W
The proposed connection of the first model	The proposed connection of the second model
The proposed connection of the third model	The proposed connection of the fourth model
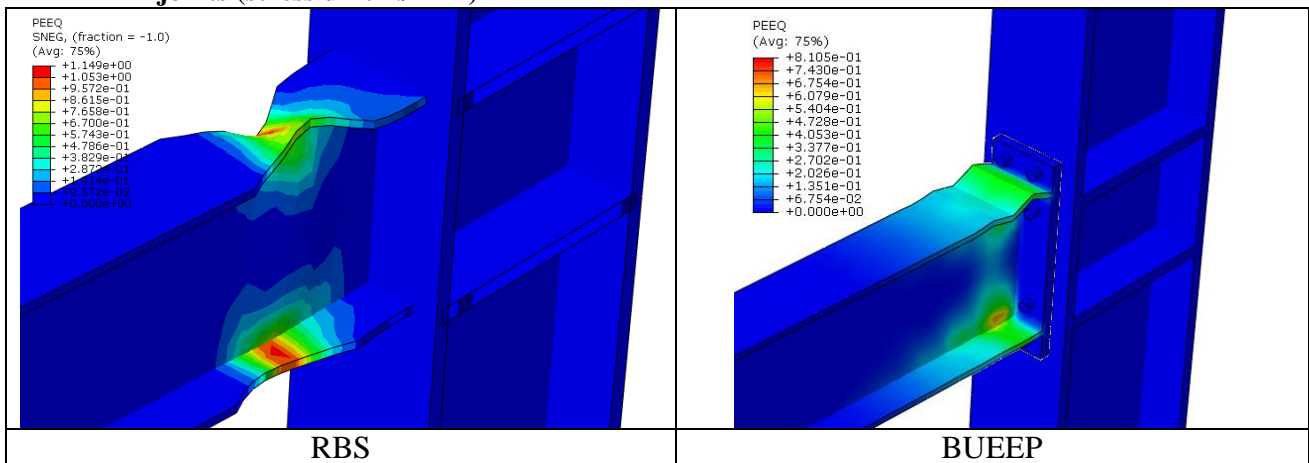
Figure 7- Equivalent plastic strain in the examined connections

By examining the stress, it can be seen that the concentration of stress in the connection between the beam and the column is higher than in other areas due to the incoming forces that include the anchor, so this area is known as the critical area of the connection. During

an earthquake, the possibility of failure in this area is very high due to high stress concentration and incoming forces. In the examined connections, the effect of stress concentration is also observed in this area. As ca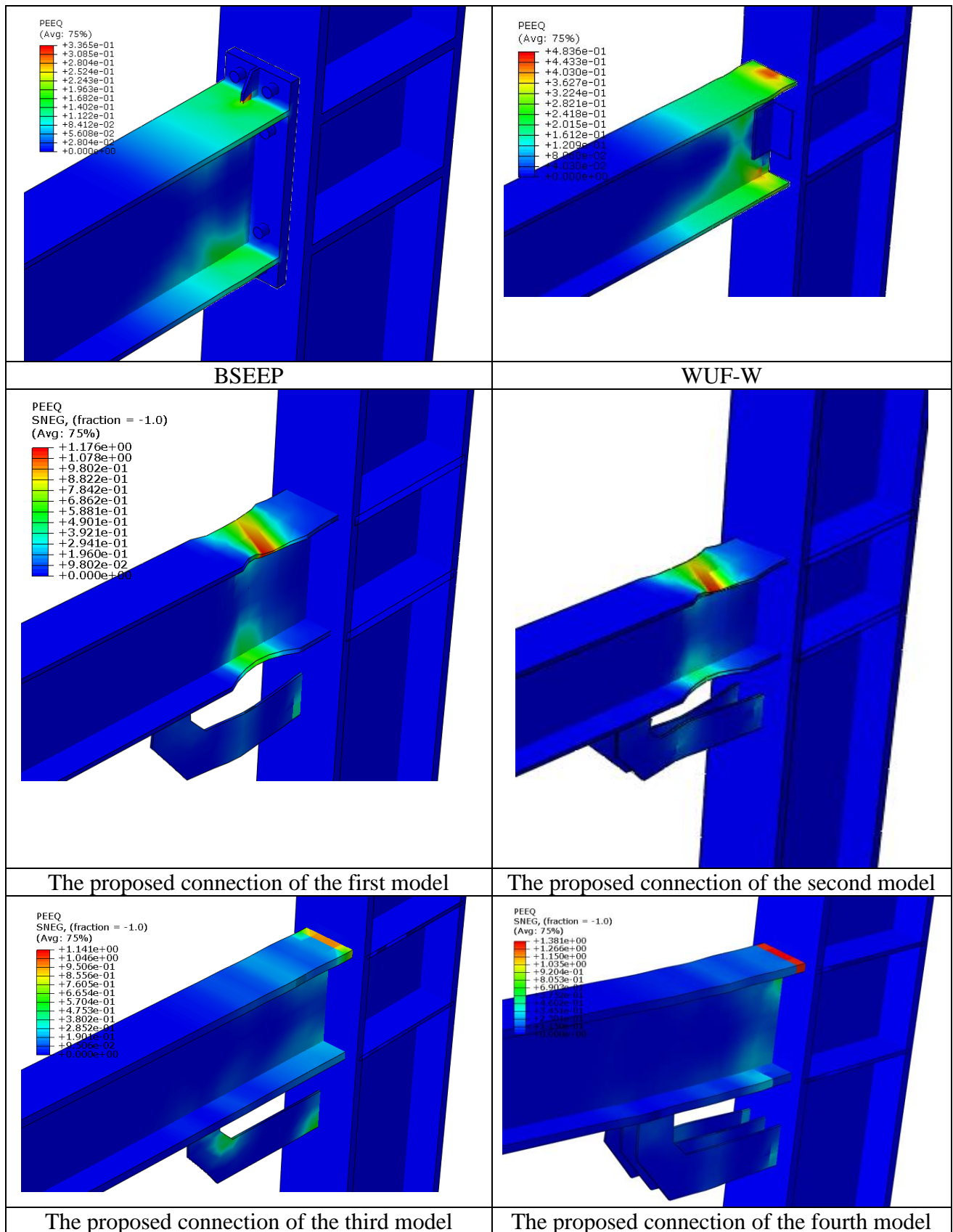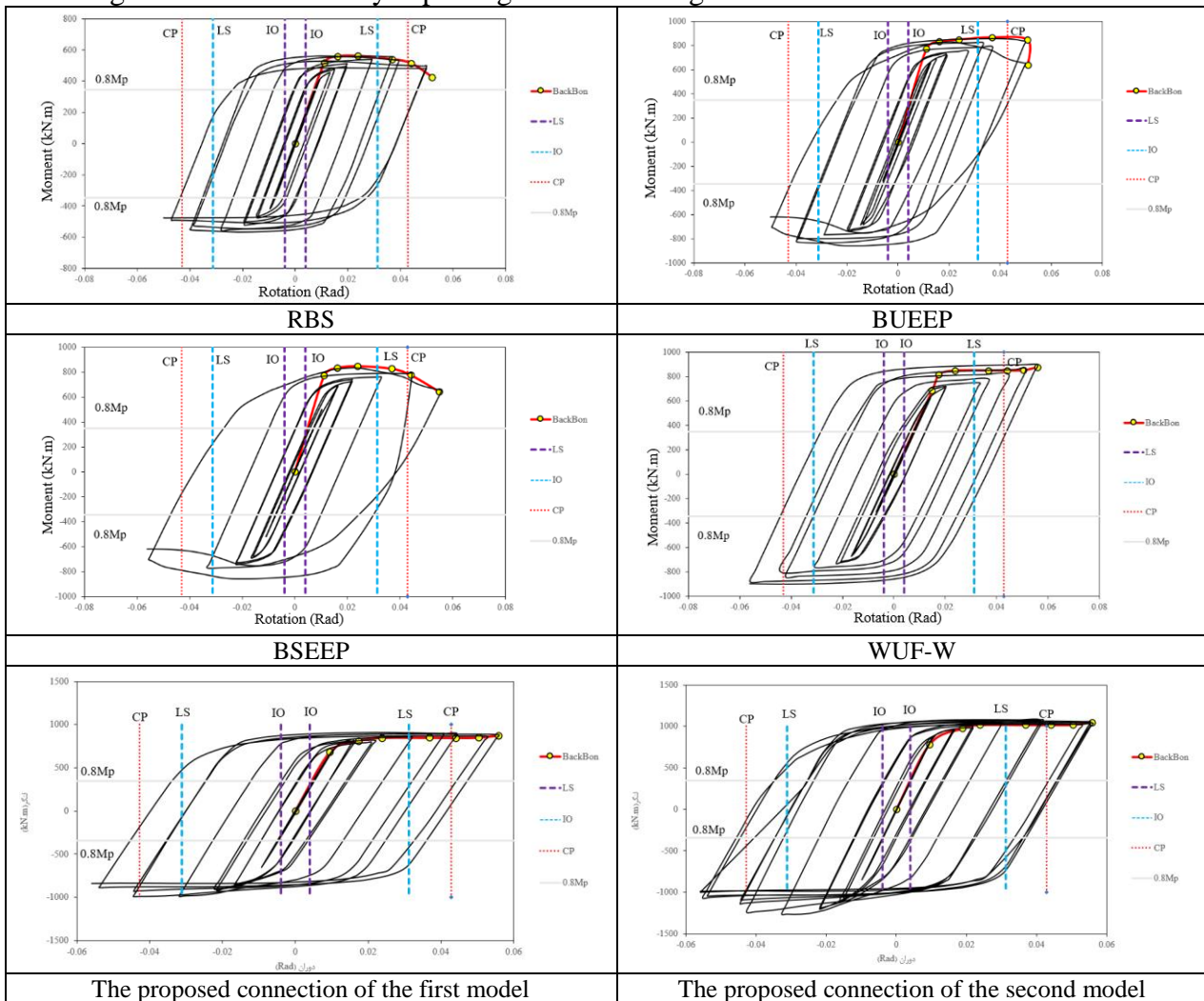n be seen in the above figures, the beam has suffered a plastic joint and failure at the connection point; this indicates that the concentration of force and stress in this part due to the bending anchor has occurred more than in other places. In this regard, it has been a very good result, because after the earthquake, the column must have the ability to bear the load, and therefore, we can rebuild and strengthen the structure by replacing the

beam. In most connections, such as the proposed connection, RBS connection, and BUEEP connection, in addition to plastic failure, we also see buckling in the beam wing. The maximum stress occurred at the joint and on the beam. The connection has worked very well. As can be seen from the figure, most of the energy absorption was on the beam. In addition, it can be seen that buckling has occurred in the stiffening area of the beam wing. In this model, the proposed part has been implemented to some extent and has absorbed a part of the energy entering the connection. Figure 8 shows the hysteresis diagram of all models.
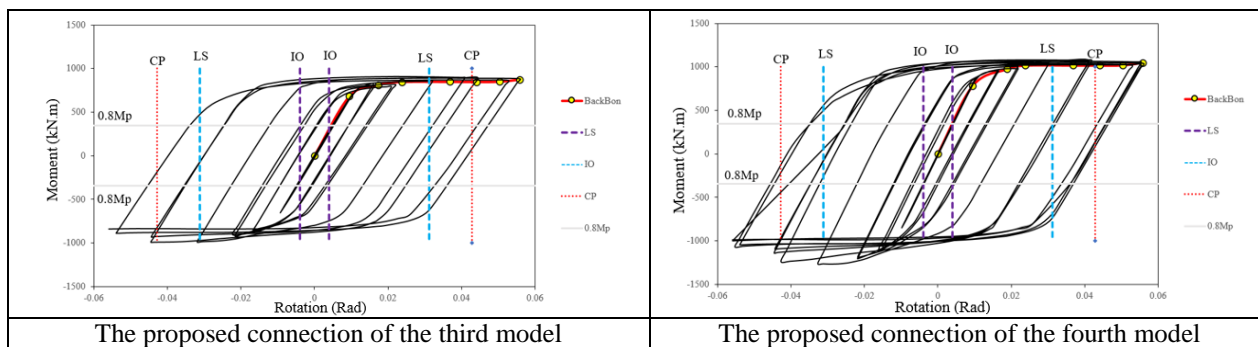

RBS

BUEEP

BSEEP

WUF-W

The proposed connection of the first model

The proposed connection of the second model

| The proposed connection of the third model | The proposed connection of the fourth model |

Figure 8- Hysteresis diagram of the studied models

As it can be seen, the structure had good resistance up to 0.04 radian of rotation and still at this point of the rotation it can withstand more than 80% bending resistance. According to the regulations, it can be seen that the structure is at the performance level of the collapse threshold. In this connection, it can be seen that the reduction of stiffness and also the initial deterioration of resistance has occurred since the rotation of 0.0038 radians, which the cause of the failure is yielding of the wing of the beam. In addition, it can be seen that the structure has yielded at a rotation of 0.0038 radians. At the rotation rate of 0.025, the stiffness is downward and it is clear that the area of the plastic joint has expanded and the reason for this was the expansion of failure in the beam and in the determined place of the connection. In addition, it can be seen that the structure has yielded at rotation of 0.0038 radians. The diagram has good plasticity and good resistance. By checking the diagrams in Figure 8, it can be seen that the desired models in the cyclic loading seen in the first figure of this section, initially the resistance increased due to the hardening behavior, but finally, the stiffness (slope of the curve) and the resistance due to the softening behavior have decreased and the curves have become slightly more relaxed than the initial state. Due to the definition of full elastic and plastic behavior for steel materials, the Bushinger effect is not observed in the diagrams, and this is due to the definition of the behavior of the materials.

4- Investigating the seismic behavior of the examined connections in the steel bending frame

In this section, two frames of one and 6 floors have been selected to check the behavior coefficient. The specifications of the selected frame are based on the described behavioral model of the connections. The investigated frames are designed in Etabs software. Finally, based on the designed sections, connections have been raised as pre-approved connections and proposed connections.

IPE is used for the column and the IPB section for the beam. ST37 steel is used for the beam and column materials. The soil is type II and it is in the seismic zone of Tehran. The structure is designed and considered in two dimensions. The proposed connection of the fourth model and the direct connection are selected for the studied frame. For modeling, the rotational stiffness of the connection is calculated in the software.

For the studied structure, live load of 1200 kg/m and dead load of 3000 kg/m are distributed on the beams. The vertical opening along the frame is assumed to be 1 meter on each side. The studied structures are considered as 1 floor. Each of the structures is modeled as a medium bending steel frame. The sections used for this 1-story structure, IPB400 is used for the column and IPE330 for the beam. The studied structures of 6-story are also modeled as a medium steel bending frame. The sections used for this 6-story structure are shown in Table 3. In the six-story structure, IPE360 is used for the first and second floors, and IPE330 columns are designed from the first to fourth floors, the third and fourth floor beams are IPE300, and the fifth and sixth floors are IPE240, and the sixth floor columns are chosen IPE270.

Table 3: Sections used for the 6-story structure

story	Beam	Column
1	IPE330	IPB360
2	IPE330	IPB360
3	IPE330	IPB300
4	IPE330	IPB300
5	IPE300	IPB240
6	IPE270	IPB240

4-1- Direct connection

Cyclic loading analysis is done. The results of this analysis are shown in the figure below. The von mises stress for direct connection is shown in Figure 9.
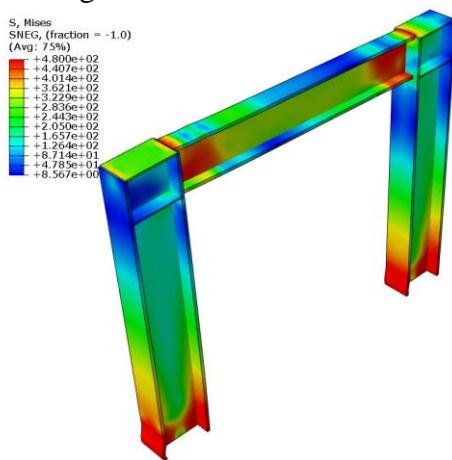

Figure 9- von mises stress in direct connection model (stress unit N/mm²)

In figure 9, the stresses correspond to the moment of maximum displacement. In the frames, due to the investigation of the behavior factor, less displacement has been applied to the structure. As a result, the stress in them is lower compared to the studied connections. As expected, the stress concentration is the highest at the connection point, and due to the placed section, the stress concentration occurred in the wing area of the beam. Figure 10 shows the equivalent plastic strain at the connection.
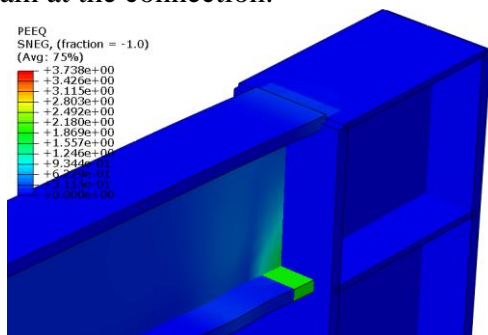

Figure 10-Plastic strain in direct connection

According to figures 9 and 10, the stress concentration created in the failure zone and the plastic joint is formed in the direct location. The hysteresis diagram of the structure is shown in Figure 11.

Figure 11- Hysteresis diagram with backbone for direct connection

In this connection, due to reciprocating loading, it can be seen that the behavior of the structure in the compression part was slightly larger in terms of the area under the curve than in the tension part, which was observed by the investigation on the frame, because the buckling in the beam has caused asymmetric and unbalanced loading to be applied to the sample.

4-2- Suggested connection

Cyclic loading analysis is done. The results of this analysis are shown in Figure 12. The von mises stress is shown in Figure 12 for the proposed connection.
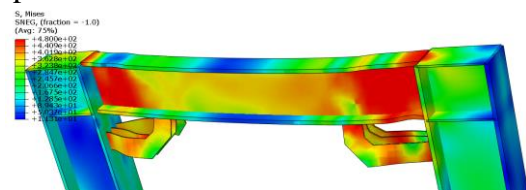
Figure 12 – von mises stress in the proposed connection model (stress unit N/mm²)

In this connection, the most stress concentration is at the connection point, and the stress concentration in the beam is higher than the column, because the base of the weak beam and strong column is observed. In addition, the additional parts add to the stiffness of the connection area. Figure 13 shows the equivalent plastic strain in the proposed connection.

Figure 13-Plastic strain in the proposed connection

In this connection, the most stress concentration is at the connection point, and this has caused the creation of a plastic joint in this area. The concentration of stress in the beam was higher than that of the column, because the base of the weak beam and the strong column were observed, and for this reason, a plastic joint was formed in the beam. The added part beneath the beam may experience buckling; therefore, in this study, the thickness of the parts has been considered slightly larger. As a suggestion for improving the results, further research can be conducted on optimizing the dimensions of this part. The hysteresis diagram of the structure is shown in Figure 14.
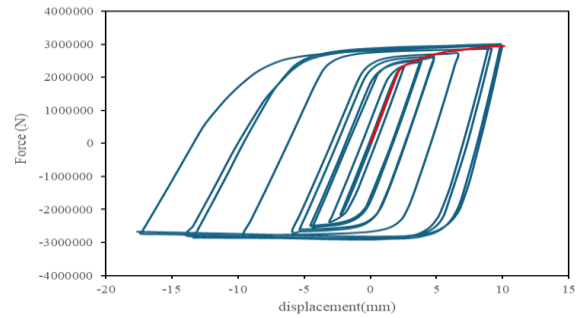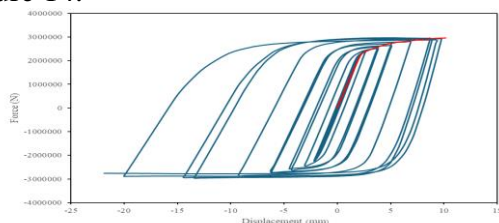

Figure 14- Hysteresis diagram with backbone for direct connection

In this connection, due to reciprocating loading, it can be seen that the behavior of the structure in the compression part was slightly larger in terms of the area under the curve than in the tension part, which was observed by the investigation on the frame, because the buckling in the beam has caused asymmetric and unbalanced loading to be applied to the sample.

5- Summary

In this section, the results are summarized. First, the results related to the bending moment are compared in Figure 15.
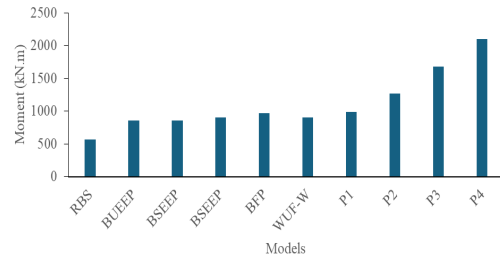

Figure 15- moment comparison

Considering that in all connections, beams and columns are the same, it can be seen from Figure 13 that the moment in the connection with the top and bottom welded flange plates (WFP) bears the highest amount of moment and the connection with the reduced surface bears the lowest amount of bending moment. In this comparison, it can be seen that the eight-bolt flanged connection using Gusset plate has endured more moment than the four-bolt flanged connection. In Figure 16, the maximum Push diagram of all models are compared.
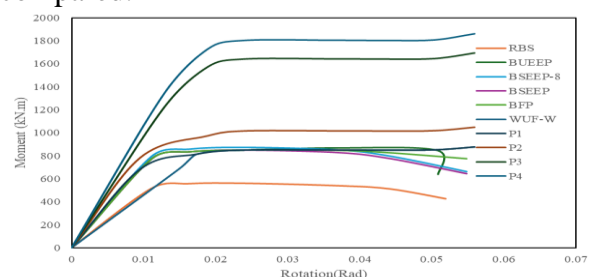
Figure 16- Comparison of Push diagram of all connections

According to Figure 16, it can be seen that the stiffness of the direct connection and the connection with the reduced wing are close to each other and the other connections are also the same. In this study, the connection with the reduced wing has the lowest amount of energy absorption among the connections. Most of the diagrams are related to the eight-screw connection. The proposed connection with an additional piece in any case has a higher capacity than the pre-approved connections due to the addition of a piece. In the table below, the coefficient of behavior of the studied frames is displayed. Table 4 shows the coefficient of behavior and parameters for calculating the coefficient of behavior of the structure.

Table 4- Calculation of behavior coefficient

		propose	direct	propose	direct

		d 1story	1story	d 6story	6story
Structure stiffness	K (N.mm)	300286.34	288737.64	1501435.9	1443689.3
extra strength	$\Omega = \Delta y / \Delta s$	2.7878	2.6818	2.9256	2.809
Plastic deformation	$\Delta u - \Delta y =$	0.4134	0.424	0.4346	0.4452
Ductility Coefficient	$\mu = \Delta u / \Delta y$	5.1834	5.2152	4.9714	5.0032
Allowable stress coefficient	$Y = \Delta s / \Delta d$	1.8656	1.7596	1.7066	1.5794
Reduction coefficient	$R\mu =$	1.8232	1.855	1.6642	1.6748
Behavior coefficient	$R = \Omega.Y.R\mu$	9.48	8.75	8.31	7.43

The explanation of these parameters of table 4:

1. Structure Stiffness (K):

   o K represents the resistance of a structure to deformation or displacement under applied loads. It is defined as the ratio of force to displacement (N/mm). Higher stiffness means greater resistance to displacement.

2. Extra Strength ($\Omega = \Delta y / \Delta s$):

   o Ω is the ratio that represents the additional strength of the structure beyond its initial elastic capacity. Δy is the yield displacement, and Δs is the elastic (linear) displacement. This parameter shows how much extra load the structure can carry before yielding.

3. Plastic Deformation ($\Delta u - \Delta y$):

   o Plastic deformation is the difference between the ultimate displacement (Δu) and the yield displacement (Δy). This represents the non-linear deformation of the structure after it has yielded, entering the plastic region.

4. Ductility Coefficient ($\mu = \Delta u / \Delta y$):

   o Ductility coefficient (μ) is the ratio of ultimate displacement (Δu) to yield displacement (Δy). It indicates the structure's ability to undergo large deformations and absorb energy without failure. Higher ductility means better performance under seismic loads.

5. Allowable Stress Coefficient ($Y = \Delta s / \Delta d$):

   o Y is the ratio between the elastic (linear) displacement (Δs) and the allowable design displacement (Δd). This coefficient indicates the structure's strength within the elastic range, comparing it to the allowable displacement limits.

6. Reduction Coefficient ($R\mu$):

   o $R\mu$ represents the reduction in seismic forces due to ductility. As the ductility of the structure increases, the seismic forces it experiences can be reduced, and this coefficient quantifies that reduction.

7. Behavior Coefficient ($R = \Omega.Y.R\mu$):

   o Behavior coefficient (R) is an overall indicator of the structure's ability to withstand seismic forces. It is the product of the extra strength factor (Ω),

the allowable stress coefficient (Y), and the reduction coefficient (Rµ). A higher behavior coefficient means the structure performs better under seismic conditions, reducing seismic forces effectively.

These parameters are crucial for assessing the performance of a structure under seismic loads and allow engineers to evaluate the structure's response to different conditions more accurately.

According to Table 4, it can be seen that the behavior coefficient of the structure with the proposed connection is higher than the direct connection, which is due to the stiffness and extra strength along with the greater ductility of the proposed connection. This trend has been repeated in the case of the six-story structure, where the behavior coefficient of the structure with the proposed connection is higher than that of the direct connection. A larger behavior coefficient reduces design sections. According to Table 3, it can be seen that the structure with the proposed connection has a higher behavior coefficient and then there is a direct connection. With the increase in the height of the structure, the behavior coefficient of the structure has also decreased.

6- Conclusion

In this study, manual calculations based on pre-approved connections of the 10th topic of the National Building Regulations of Iran, as well as numerical modeling in Abaqus finite element software, have been investigated. In order to compare the behavior, first the connection is designed based on what is proposed in the 10th topic of the National Building Regulations. After designing the connection, all its components have been modeled and studied in Abaqus finite element software according to what is designed in the manual part. In order to check the behavior of the connection, it has been subjected to cyclic loading by software, and finally, the plastic joint and the hysteresis diagram of this connection have been drawn and compared. Based on the results obtained from manual and numerical analysis based on Abaqus finite element software, the following results can be mentioned.

Based on the studies conducted in this paper, the following results have been obtained.

• According to the software models, it can be seen that in all the models, the bending moment capacity of the connection is more than 40% of the calculated plastic moment in the connection. In connection with the reduced cross-section, this percentage has reached nearly 20%.

• Based on the numerical results, it can be seen that the bending capacity of the 8-bolt flanged connection and the connection with the top and bottom welded flange plates is more than the rest of the studied connections.

• In the connection with a reduced cross-section, because the cross-section has been reduced, the bending moment capacity is lower than the rest of the studied connections.

• The results of the proposed connection behavior show that it performs nearly 25-34% better than the pre-validated connection of the 10th topic.

• The structure with the proposed connection has a higher coefficient of behavior than a direct connection. This shows that the structure with the proposed connection of sections will be more suitable and economical. The value of the coefficient of behavior in the structure with the proposed connection is approximately 11% in the 6-story structure and 9% in the 1-story structure more than the structure with the pre-validated connection.

• With the increase in the height of the structure, the coefficient of behavior of the structure has also decreased.

• In most of the examined joints, it is observed that considering that the structure has reached the threshold of collapse, but still the bending strength of the connection was suitable and the stiffness of the structure has decreased in the threshold of collapse, but the decrease was not complete, It is with a gentle slope.

• It can be seen that the reduction of hardness and also the initial deterioration of resistance occurred from the rotation of 0.0038 radians in these examined connections. This value has been almost the same in all joints and the beginning of the reduction of hardness is predicted at this point for most of the joints.

Based on the results, it can be seen that the proposed connection has improved the behavior of the steel bending frame, and it can be seen from the hysteresis diagram of the structure that the diagram has an increasing trend, and this is a sign of the additional piece on the connection. which has increased the stiffness of the connection as well as the steel bending frame.

• The area under the curve of the bending frame with the proposed connection is almost 10% higher than the steel bending frame with the pre-approved connection. This is due to the resistance and also the greater hardness of the proposed connection.

Refrences

1. Hanson, N.W., Conner, H.W., "Seismic Resistance of Reinforced Concrete BeamColumn Joints", Journal of Structural Division, ASCE, V. 93, ST. 5, Oct 1967.

2. Ehsani, M. R. and Wight, J. K., "Exterior Reinforced Concrete Beam to Column Connection Subjected to Earthquake-Type Loading", ACI journal, pp. 402- 499, 1985.

3. Durrani, A. J., and Wight, J. K., "Experimental and Analytical Study of Internal Beam to Column Connections Subjected to Reversed Cyclic Loadings", Report No. UMEE 82R3, Department of Civil Engineering, University of Michigan, Ann Arbor, Mich., 275, 1982.

4. ACI-ASCE Committee 352, "Recommendations]9[for Design of Beam Column Joints in Monolithic Reinforced Concrete Structures", ACI Journal, Vol. 82, No. 3, pp. 266- 283, May- June 1985. ACI-ASCE Committee 352, Recommendations]10[for design of Beam-Column Joints in Monolithic Reinforced Concrete Structures, ACI 352R- 91, Re-approved, 1997.

5. Li, L., Wang, W., Chatzi, E., & Ghafoori, E. (2023). Experimental investigation on debonding behavior of Fe-SMA-to-steel joints. *Construction and Building Materials*, *364*, 129857.

6. Mohabeddine, A., Malik, G., Correia, J., Silva, F., De Jesus, A., Fantuzzi, N., & Castro, J. M. (2023). Experimental parametric investigation on the behavior of adhesively bonded CFRP/steel joints. *Composite Structures*, *307*, 116598.

7. Ha, G. J., Kim, J. K. and Chung L.,"Response of Reinforced High-Strength Concrete BeamColumn Joints Under Load Reversals", Magazine of Concrete Research, Vol. 44, No. 160, pp. 175- 184, 1992.

8. Houshmand-Sarvestani, A., Totonchi, A., Shahmohammadi, M. A., & Salehipour, H. (2023). Numerical assessment of the effects of ADAS yielding metallic dampers on the structural behavior of steel shear walls (SSWs). *Mechanics Based Design of Structures and Machines*, *51*(3), 1626-1644.

9. Li, J., Wang, Y., Zhang, Z., & Mou, B. (2023). Seismic behavior of steel frames with different joints: Shaking table test and finite element analysis. *Journal of Building Engineering*, *70*, 106377.

10. Ganesan, N., Indira P.V. and Abraham, R., "Steel Fiber Reinforced

High Performance Concrete Beam-Column Joints Subjected to Cyclic Loading", ISET Journal of Earthquake Technology, Vol. 44, No. 3- 4, , pp. 445– 456, Sept. Dec, 2007

11. Shannag, M.J., Abu-Dyya, N. and Abu-Farsakh, G., "Lateral Load Response of HighPerformance Fiber Reinforced Concrete Beam-Column Joints", Construction and Building Materials,Vol. 19, No. 7, pp. 500–508, 2005.

12. Roudsari M Tahamouli, Jamshidi H, Moradi SH. Experimental and numerical assessment of reduced IPE beam sections connections with box-stiffener. Int J Steel Struct 2018;18(1):255–63.

13. Sang .JuL.EE , Sang. E. H. , Sam Y. N. , Sung .W. S.," Deformation Capacity of Reduced Beam Section Moment Connection by Staggered Holes" , Proceedings of the International Conference on Sustainable Building Asia, Seoul, Korea, 27 29 June 2007.

14. Farrokhi. H., Danesh. F., Eshghi. S., "A modified moment resisting connection for ductile steel frames (Numerical and experimental investigation)"Journal of Constructional Steel Research 65 (2009) 2040–2049.

15. Shahu, A., Hiwase, P. D., Choudhari, A. S., & Shangondawar, M. (2020). Comparison on Sustainability of Moment Resistance Connection Methods in Steel Design. Helix, 10(01), 200-203..

16. American Institute of Steel Construction (AISC). " Seismic Specifieation for Structural Steel Buildings" Chicago . IL. (2005).

17. FEMA -355 D. ," State of Art Report on Connection Performance " , Prepared by the SAC Joint Venture for the Federal Emergency Management Agency , Washington ,September , 2000.

18. El-Tawil ,S., Mikesell . T.,Vidarsson. E., and Kunnath. SK .," Strength and ductility of FR Welded-bolted Connection" ,SAC Report 98-1 .sacramento ,calif ., SAC Joint Venture 1998.

19. Shin, Kyung-Jae, Young-Ju Kim, and Young-Suk Oh. "Seismic behaviour of composite concrete-filled tube column-to-beam moment connections." Journal of Constructional Steel Research 64, no. 1 (2008): 118-127.

20. Wang, P., Wang, Z., Pan, J., Zheng, Y., & Liu, D. (2019). Cyclic Behavior of Steel Beam to CFT Column Connections with Gusset Plates. Advances in Civil Engineering, 2019.

21. Krawinkler, H., Bertero, V., Popov, E.P,. Inelastic behavior of steel beam-to-column subassemblages. Earthquake Ebgineering Research Center. 1971.

In the present study, an actual three-dimensional (3D) steel building, with one Lead Rubber Bearing (LRB) seismic isolation device under each column, has been investigated. The considered building is used as a school located at the high damage risk zone. Therefore, health monitoring of this structure is plausible. The aforementioned building is an actual 5-story steel building with an irregular plan, and the Load Resistance Factor Design (LRFD) algorithm was used for the design procedure based on

the American Institute of Steel Construction (AISC) code [19]. This building is equipped with a total number of 67 LRBs in its isolation base under each column. A 3D view of the FE model is depicted in Figure 1.

The most common base isolation devices used over many years by engineers are LRB isolators which combine isolation function and energy dissipation in a single compact unit [20-21]. Such LRB isolator devices provide vertical load support, horizontal flexibility, supplemental damping, and centering force to the structure from earthquake attack. In addition, they require minimal cost for installation and maintenance as compared to other passive vibration control devices [22-23]. The LRB isolator is composed of an elastomeric bearing made by laminated rubber layers with steel shim plates, cover plates, and a lead core located on its center. The typical LRB isolator device is shown in Figure 2. The typical LRB isolator has considerable maximum shear strains corresponding to between 125% and 200% because reinforcing steel plates have little effect on the shear stiffness. This LRB isolator device can combine the function of isolation and recentering in a single unit (*i.e.*, elastomeric bearing), thereby giving structural support, horizontal flexibility, and recentering force to the isolation system [24-25]. Furthermore, it produces the required amount of supplemental damping and energy dissipation by adjusting the size of the lead core. The energy dissipation generated by the yielding of the lead core achieves an equivalent viscous damping coefficient up to approximately 30%, and effectively reduces the horizontal displacement. The LRB isolators are usually fabricated in circular sections, and sometimes produced with more than one lead core. A LRB model practically used in the construction field is selected in this study. Including geometric details illustrated in Figure 2, mechanical properties needed to simulate their force-displacement responses are presented in Table 1. As shown in Figure 3, the force-displacement responses can be ideally modeled as bilinear hysteresis loops. The bilinear hysteresis loops considered herein are defined as four key parameters given in Table 1 per each LRB model, such that: yield displacement ($\Delta 1$), yield force ($F1$), specified design displacement ($\Delta 2$), and its corresponding force ($F2$). The elastic stiffness (Ke) and the post-yield stiffness (Kp) are defined as Equations (1) and (2).
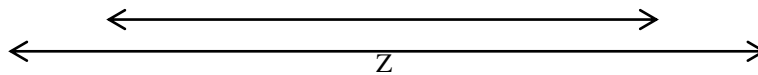
Fig. 1. The 3D view of FE structural model

١٨

Z
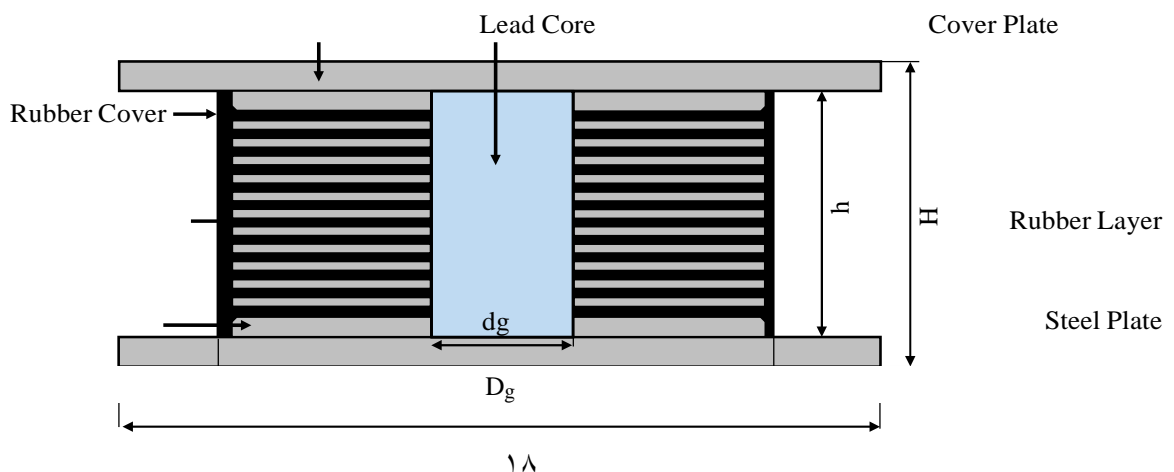
Fig. 2. Typical LRB isolator device

Table 1. Properties of the LRB isolator model

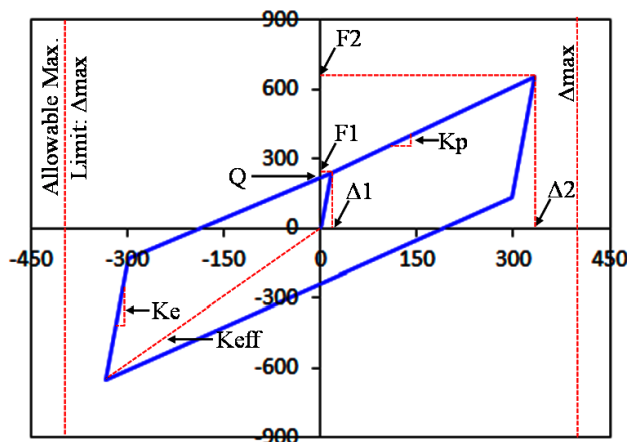| characteristic	Δmax	Fv	F1	F2	Δ1	Δ2	Q	Ke	Kp	Keff	λeff	Z	Dg	dg	H	h	te *
Unit	mm	kN	kN	kN	mm	mm	kN	kN/m	kN/m	kN/m	mm	mm	mm	mm	mm	mm	mm
Value	400	3170	259	651	16	333	239	16.19	1.24	1.95	22.3%	800	750	170	397	337	203

* Total thickness of the rubber

Fig. 3. Hysteresis loop of the presented LRB isolator device modeled as bilinear curves

(1) $K_e = \dfrac{F1}{\Delta 1}$

(2) $K_p = \dfrac{F2 - F1}{\Delta 2 - \Delta 1}$

The effective stiffness of the hysteretic behavior ($Keff$) can be modeled the secant line by means of the ratio as Eq. (3).

(3) $K_{eff} = \dfrac{F2}{\Delta 2}$

The characteristic strength indicating force-intercept at the zero displacement (Q) can be alsoexpressed as the function of the post-yield stiffness as Eq. (4).

(4) $Q = F1 - K_p.\Delta 1$

The hysteretic loop area ($Eiso$) representing the amount of energy dissipation can be obtained from Eq. (5).

(5) $E_{iso} = 4Q.(\Delta 2 - \Delta 1)$

The effective viscous damping coefficient (λeff) is proportional to the amount of energy dissipation, but inversely related to both the effective stiffness and the square displacement. This damping coefficient also depends on four key parameters, which it refers:

(6) $\lambda_{eff} = \dfrac{E_{iso}}{2\pi.K_{eff}.(\Delta 2)^2} = \dfrac{2}{\pi}\left(\dfrac{F1}{F2} - \dfrac{\Delta 1}{\Delta 2} \right)$

The mechanical properties obtained from calculations in the above equations are summarized in Table 1.
LRB has the maximum allowable horizontal displacement ($\Delta max = 400$ mm), representing 1.2 times the length of $\Delta 2$.

4. Verification

The verification of this novel approach was performed by statistical comparison between achieved results with Saiful Islam et al.'s [26] research on base isolation system. In this research a non-linear time domain analysis was also performed by choosing the proper ground motion that scaled with the site condition of Dhaka city in Bangladesh. The comparison between this study and Saiful Islam et al.'s research for top floor acceleration in X and Y direction with scatter plots are shown in Figure 4. There are good agreements between this study and the reference research (R^2=0.963 in X direction and R^2=0.975 in Y direction). In this regards, the novel approach has good accuracy to discretize governing equation for NTA.
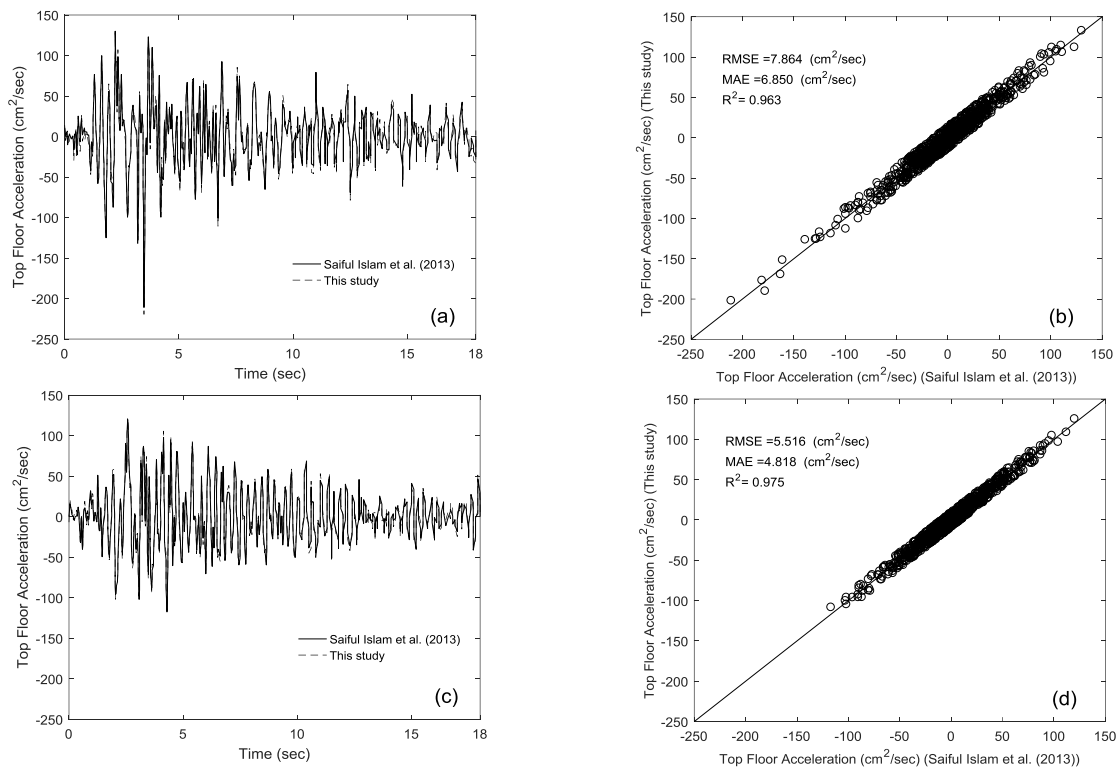

Fig. 4. Top floor acceleration Time History, a) X direction, b) scatter plot in X direction, c) Y direction, d) scatter plot in Y direction

5. Analysis Procedure

5-1- Modal analysis

Natural frequencies are the important characteristics of a structure. It can be used to analyze the results that obtained by dynamic analysis. The vibration properties were calculated by performing MA. Table 2 presents the first six natural time periods and maximum modal responses of the proposed model. Figure 5 illustrates the first six mode shapes of the BI structure. It was often necessary to consider more fundamental modes in order to take account for 90% of the modal mass [27].

Table 2. Modal analysis results; periods and maximum displacements

Mode no.	Period (s)	Max Dis. (x cm)	Max Dis. (y cm)	Max Dis. (z cm)
1	4.01	0.037	0.039	0.03
2	3.89	0.036	0.038	0.029
3	3.26	0.03	0.033	0.026

4	1.07	0.019	0.026	0.017
5	1.04	0.018	0.025	0.015
6	0.919	0.016	0.023	0.014

5-2- Nonlinear time history analysis

One of the most important challenges in analyzing irregular structures is considering the effects of earthquakes on structural responses. Some scientists have raised special concerns as to ordinary buildings that are vulnerable to strong impulsive NF ground motions [28-30]. The NF ground motions recording from recent earthquakes are different from general ground motions in that they contain a strong-narrow band pulse of the spectral acceleration at short to intermediate periods [31-33]. Once ordinary frame buildings with relatively short vibration periods undergo these NF ground motions, inter-story drifts generated tend to be considerable due to strong ground acceleration pulses delivered into the column bases [34-37]. In this study, in order to select the appropriate earthquake records based on three criteria of magnitude, distance, and type of soil, the TOPSIS method is used [38]. Three sets of recorded earthquake ground motions including NF seismic records were considered in NTH. The parameters of the selected ground motion records are given in Table 3. Responses of structure were obtained in x, y and z directions. The evidences in Table 4 have been attained from dynamic analysis of the presented BI building. The time histories obtained are maximum base shear, base moment and displacements. As sample of performed analysis, Figure 6 illustrates the results of NTH under the Landers earthquake (1992).

Table 3. The used seismic ground motion records

Earthquake	Record ID	Magnitude (Mw)	PGA (g)	Site Classification
Landers (1992)	LADSP000	7.5	0.17	C
San Fernando (1971)	P0052	6.6	0.174	C
Northridge (1994)	NRORR360	6.8	0.51	C

Table 4. Maximum results of nonlinear time-history analyses for a BI structure subjected to near-fault earthquakes

Earthquake	Design base shear (kN) in x direction	Design base shear (kN) in y direction	Design base moment (kN-m) in x direction	Design base moment (kN-m) in y direction	Roof-story displacement (cm) in x direction	Roof-story displacement (cm) in y direction
Landers (1992)	2842	1956	38293	26228	7.98	7.89
San Fernando (1971)	2733	1869	37395	26004	7.01	6.68
Northridge (1994)	2779	1896	37786	26108	7.44	7.08

(a)

(b)

(c)

(d)

(e)

(f)
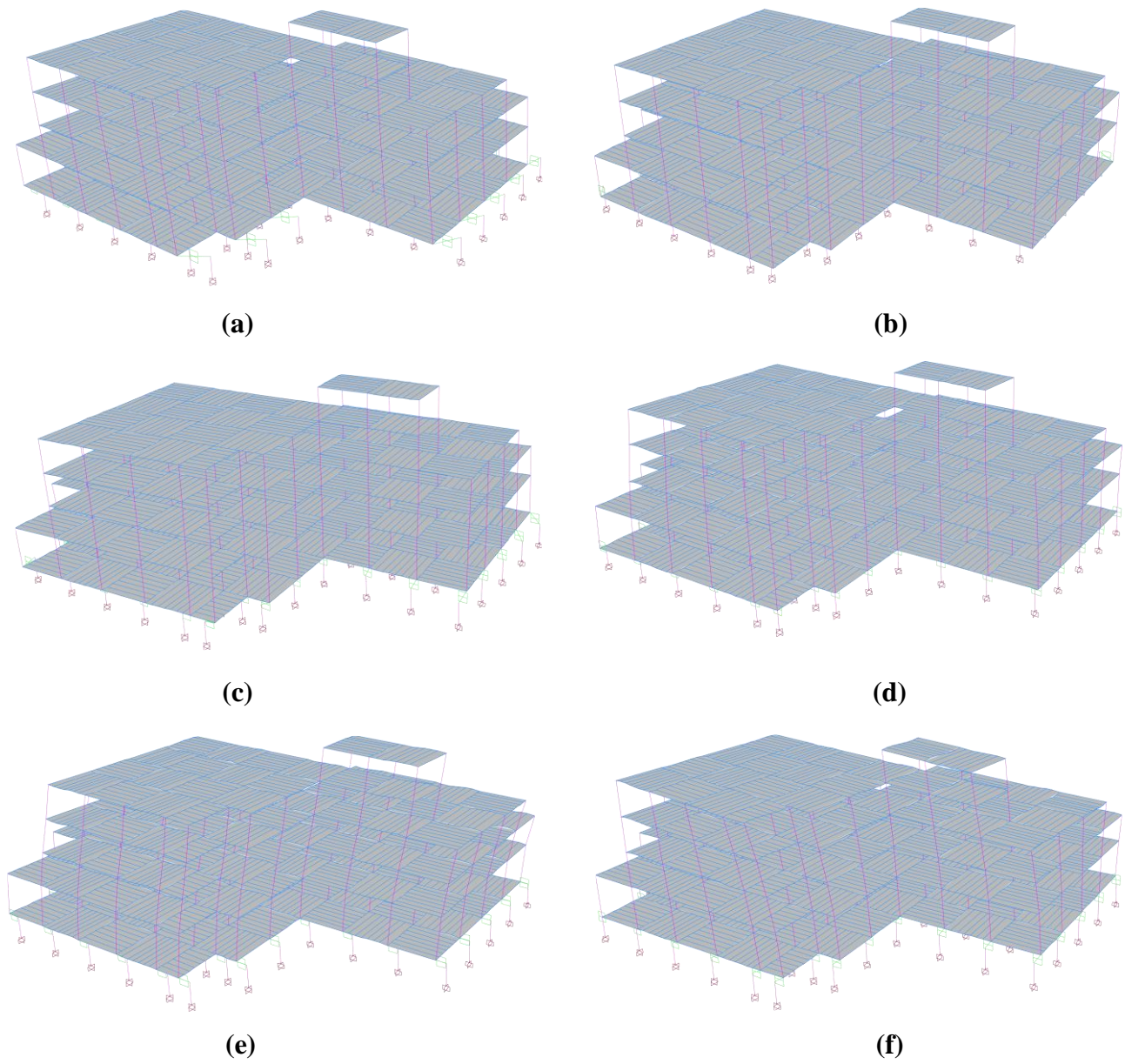
Fig. 5. Mode shapes of BI structure   **(a) 1ˢᵗ**   **(b) 2ⁿᵈ**   **(c) 3ʳᵈ**   **(d) 4ᵗʰ**   **(e) 5ᵗʰ**   **(f) 6ᵗʰ**

(a)

(b)

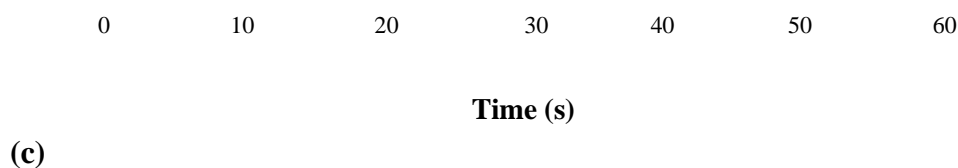0   10   20   30   40   50   60

Time (s)

(c)
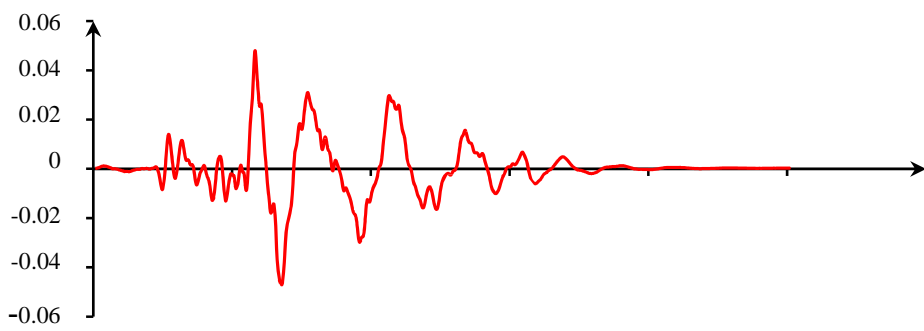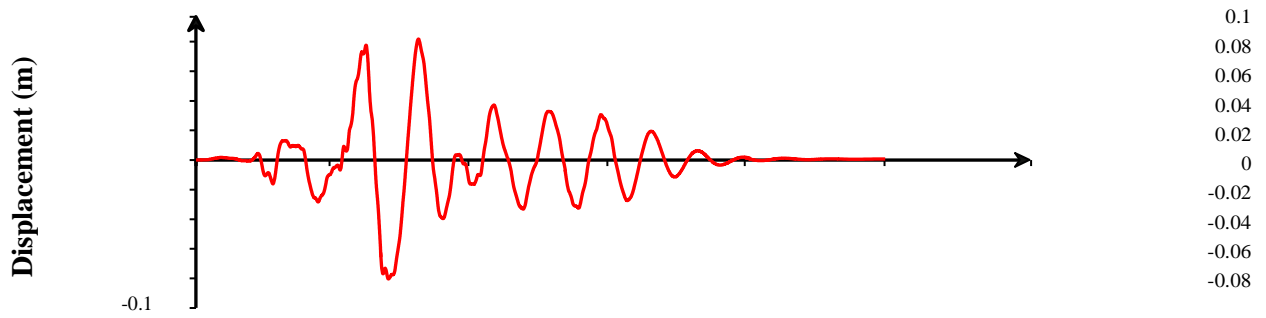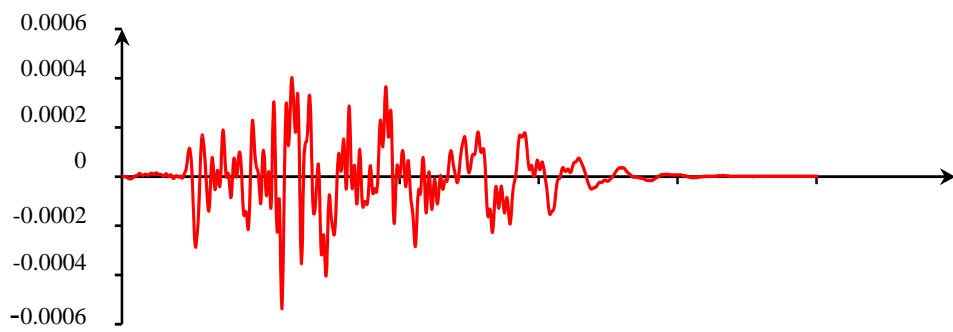
**Fig. 6. Displacement time-history of the BI system subjected to Landers earthquake (1992)
(a: longitudinal, b: transverse, c: vertical components)**

6. Genetic Algorithm

To find the optimal solution of the objective function, the GA is used. The GA is well known due to its simplicity and robustness in the solution of complex problems so that these characteristics fit well to the problem described in this paper [39]. GAs have been widely used in sensor placement type problems [40].

The GA has been proved to be a powerful tool in the OSP; however, it has some faults that need to be rectified. For example, one sensor location may be placed where two or more sensors exist or sensor numbers are not equal to a certain number [41]. A good surveillance system must detect the aftermath of a contaminant spill as soon as possible with maximum reliability. Earlier detection gives more time to the system managers to react. Thus, an objective of the optimization is to maximize the detection time that can be defined in an average sense and an objective function.

In this optimization method, information about a problem, such as variable parameters, is coded into a genetic string known as a chromosome. Each of these chromosomes has an associated fitness value, which is usually determined by the objective function [42].

7. OSP process

Numerous techniques have been advanced for the OSP problem and were widely reported in the literature. These have been developed using a number of approaches and criteria, some are based on intuitive placement or heuristic approaches, and others may employ systematic optimization methods. The sensor placement optimization can be generalized as "given a set of n candidate locations, find the subset of m locations, where $m \leq n$, which may provide the best possible performance" [43].

As known, the measured mode shape vectors in the SHM have to be as possible linearly independent, which is a basic requirement to distinguish, measured or identified modes. In this research, three different OSP algorithms are utilized which include MAC, extended MAC (EMAC) and TTFD.

7-1- MAC approach

All the past studies have been developed based on intuitive placement, heuristic approaches, and systematic optimization methods. The MAC is a mathematical criterion to check the compatibility between two eigenvectors. MAC matrix is defined as Eq. (7) [2-3].

$$(7) \quad MAC_{ij} = \frac{(\phi_i^T \phi_j)^2}{(\phi_i^T \phi_i)(\phi_j^T \phi_j)}$$

Where ϕ_i and ϕ_j represent the ith and $j$the column vectors in matrix ϕ, respectively, and the superscript T denotes the transpose of the vector. In this equation, the MAC values fall

within the range between 0 and 1. Zero value of MAC shows lack of any correlation between the off-diagonal element of matrix and one indicates a high degree of likeness between the modal vectors. Then, the maximum values of mode displacements for nodes corresponding to the maximum off-diagonal terms with Square-Root-of-Sum-of-Squares (SRSS) or Complete Quadratic Combination (CQC) were calculated. First, these points are selected for initial placement of sensors. Second, it adds other available candidate sensors one by one, and selects one that minimizes the maximum off-diagonal element of the MAC matrix at each step. Therefore, the MAC objective function is defined as Eq. (8).

$$(8) \quad f = 1 - max\big(abs\big(MAC_{ij}\big)\big)$$

This objective function is used to determine the highest MAC values for identifying the critical modes with similar motions. Next, the MAC repeats the second step by adding one sensor at a time until a required number of sensors are selected. The locations selected for the five accelerometers needed to be installed. It should be noticed that due to the nature of the GA method, the results are usually dependent on the randomly generated initial conditions, which means the algorithm may converge to a different result in the parameter space. These values are very close to the optimal value.

7-2- EMAC algorithm

To overcome the contra-decreasing problem of the original MAC algorithm, a forward-backward combinational extension was developed as follows by Li [8]. An EMAC algorithm was proposed to overcome the disadvantages of traditional MAC algorithm with the introduction of a forward-backward combinational approach. First, an intuition sensor set, U_0 (including, to say, a number of sensors, s_0) is chosen. Then, one sensor is added to this initial set until a preset number of sensors, which is somewhat larger than the number of sensors as required, for instance, ten percent more than required ($1.1 \ s_0$), is reached. This is the same as the forward sequential MAC procedure. The extension differs from the original forward approach in the stopping criterion. The EMAC algorithm is continued to obtain a sensor set, U_1, consisting a certain number of sensors (to say, s_1, $s_1 \le 1.1 s_0$) larger than the required one, s_0, where the original stops.

Secondly, one sensor at each step is excluded from the sensor set U_1 until the required number of sensors s_0 is reached. This is the backward sequential MAC approach, the essential extension to the forward one. Therefore, two function curves are established. One is the curve of the maximum off-diagonal term with respect to the number of sensors increasing from s_0 to s_1, which is obtained in the first stage, and the other is the curve of the maximum off-diagonal term with respect to the number of sensors decreasing from s_1 to s_0, which is found in the second stage. Both curves are compared and the one with a smaller value at the point s_0 is selected. Which curve is to be selected, depends on the abilities of the forward and backward approaches to minimize the maximum off-diagonal terms of the MAC matrix. In this manner, the maximum off-diagonal term of the MAC matrix may, in many instances, be further minimized than the traditional MAC algorithm. Naturally, the forward stopping number of sensors s_1 in the first step can be varied according to the structure under consideration. The effects of various numbers s_1 of sensors on the selection set (including s sensors) of the above two step processes can be compared and the one with the smallest maximum off-diagonal term of the MAC matrix can be chosen. This can be implemented as the third step, if necessary. There is one note about the influence of the choice of the intuition sensor set, U_0, on the final selection of sensor positions. If a newly added sensor conflicts with one or several of the original intuition set, the intuition set may be reformed if the exclusion of certain sensor from the original intuition set U_0 is not

considered to be much detrimental to the mode shape visualization. Afterwards, the two steps can be recomputed. Tables 5 and 6 demonstrate the values assigned to reproduction parameters and the attained fitness values for MAC and EMAC algorithms. Figure 7 illustrates the MAC matrixes of reduced sensor locations based on MAC and EMAC algorithms.

Table 5. The values of GA parameters (MAC)

Population	Elite individuals	Crossover individuals	Mutation individuals	Fitness value
100	31	50	22	1.08

Table 6. The values of GA parameters (EMAC)

Population	Elite individuals	Crossover individuals	Mutation individuals	Fitness value
100	36	50	27	1.31
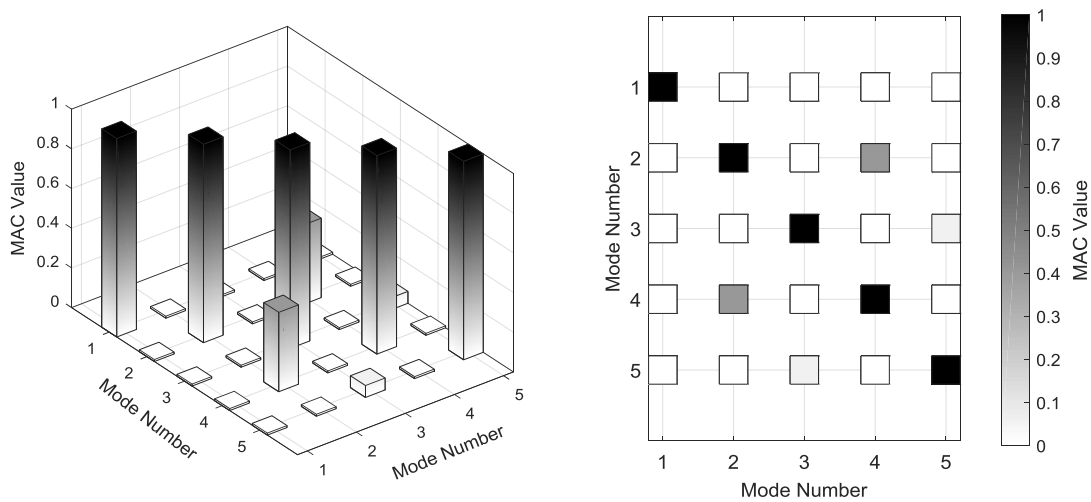
(a)
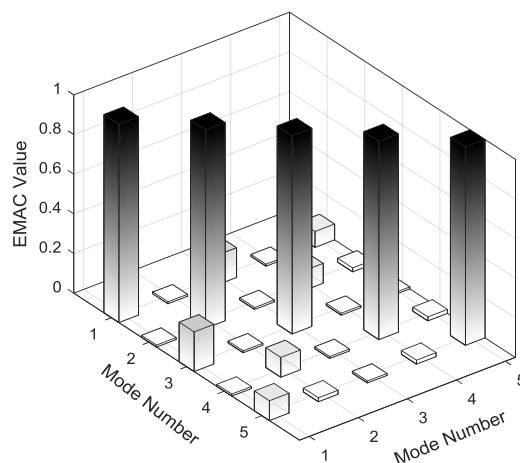
(b)

Fig. 7. The MAC matrix of reduced sensor locations based on a) MAC b) EMAC algorithms

7-3- TTFD (modified MAC) algorithm

Any signal can completely be described in time or frequency domain, and so, the equivalent periods T_{ei} are obtained [44]. Both representation data in time or frequency domain can transform to each other. These transformation, the so-called Fourier Transformation and the Inverse Fourier Transformation, are given in Equations (9) and (10), respectively.

$$U(\omega) = \int_{-\infty}^{+\infty} u(t).e^{-i\omega t} dt \qquad (9)$$

$$u(t) = \frac{1}{2\pi} \int_{-\infty}^{+\infty} U(\omega).e^{i\omega t} d\omega \qquad (10)$$

There was no precisely dynamic response on the past presented OSP algorithms, and the authors of this article developed the TTFD algorithm on the basis of NTA. The mathematical process of TTFD is given by

Eq. (11). In first step of this approach, the results of the non-linear analysis were used in order to obtain the exact sensors placement. The values of displacement-time output results in time domain must be transformed to frequency-domain in the second step of this approach based on Eq. (10). In the next step of TTFD approach, the effective frequencies according the maximum Fourier amplitude were selected. In fourth step of this method, the normalized seismic displacement of each effective period was considered. In this respect, these normalized displacement in Z ($j=1: n$) direction act as mode shape in MAC analysis. In this equation, n is the number of levels of dam considered to install the fiber Bragg grating (FBG) sensors. The modified type of MAC values can be obtained from MAC in the last step of this approach.

$$t_i = \begin{Bmatrix} t_1 \\ t_2 \\ t_3 \\ \vdots \\ t_n \end{Bmatrix} \xrightarrow{Step1} u(t)_i = \begin{Bmatrix} u(t)_1 \\ u(t)_2 \\ u(t)_3 \\ \vdots \\ u(t)_n \end{Bmatrix} \xrightarrow{Step2} U(\omega)_i = \begin{Bmatrix} U(\omega)_1 \\ U(\omega)_2 \\ U(\omega)_3 \\ \vdots \\ U(\omega)_n \end{Bmatrix} \xrightarrow{Step3} f_{ei} = \begin{Bmatrix} f_{e1} \\ f_{e2} \\ f_{e3} \\ \vdots \\ f_{en} \end{Bmatrix} \Rightarrow T_{ei} = \begin{Bmatrix} T_{e1} \\ T_{e2} \\ T_{e3} \\ \vdots \\ T_{en} \end{Bmatrix}$$

$$(11)$$

$$T_{ei} = \begin{Bmatrix} T_{e1} \\ T_{e2} \\ T_{e3} \\ \vdots \\ T_{nen} \end{Bmatrix} \xrightarrow{Step4} u(z)_{ei} = \begin{Bmatrix} u_{j(z)e1 \ j=1\to n} \\ u_{j(z)e2 \ j=1\to n} \\ u_{j(z)e3 \ j=1\to n} \\ \vdots \\ u_{j(z)nen \ j=1\to n} \end{Bmatrix} \& \quad u(x)_{ei} = \begin{Bmatrix} u_{j(x)e1 \ j=1\to n} \\ u_{j(x)e2 \ j=1\to n} \\ u_{j(x)e3 \ j=1\to n} \\ \vdots \\ u_{j(x)nen \ j=1\to n} \end{Bmatrix} \xrightarrow{Step5} Modified\ MAC$$

In this study, a novel approach of OSP algorithms with combination between MAC and TTFD were utilized. The CQC method was utilized as a famous modal combination technique. However, after the time frequency transformation, the corresponded values of time history analysis should be substituted with the MA outcomes. Hence, all of the required parameter values in the CQC such as

maximum modal responses are replaced with transformed equivalent time histories results. As sample of carried out analysis, Figure 8 illustrates the response acceleration-time diagram of Landers earthquake (1992) and corresponded time-frequency domain transformation.
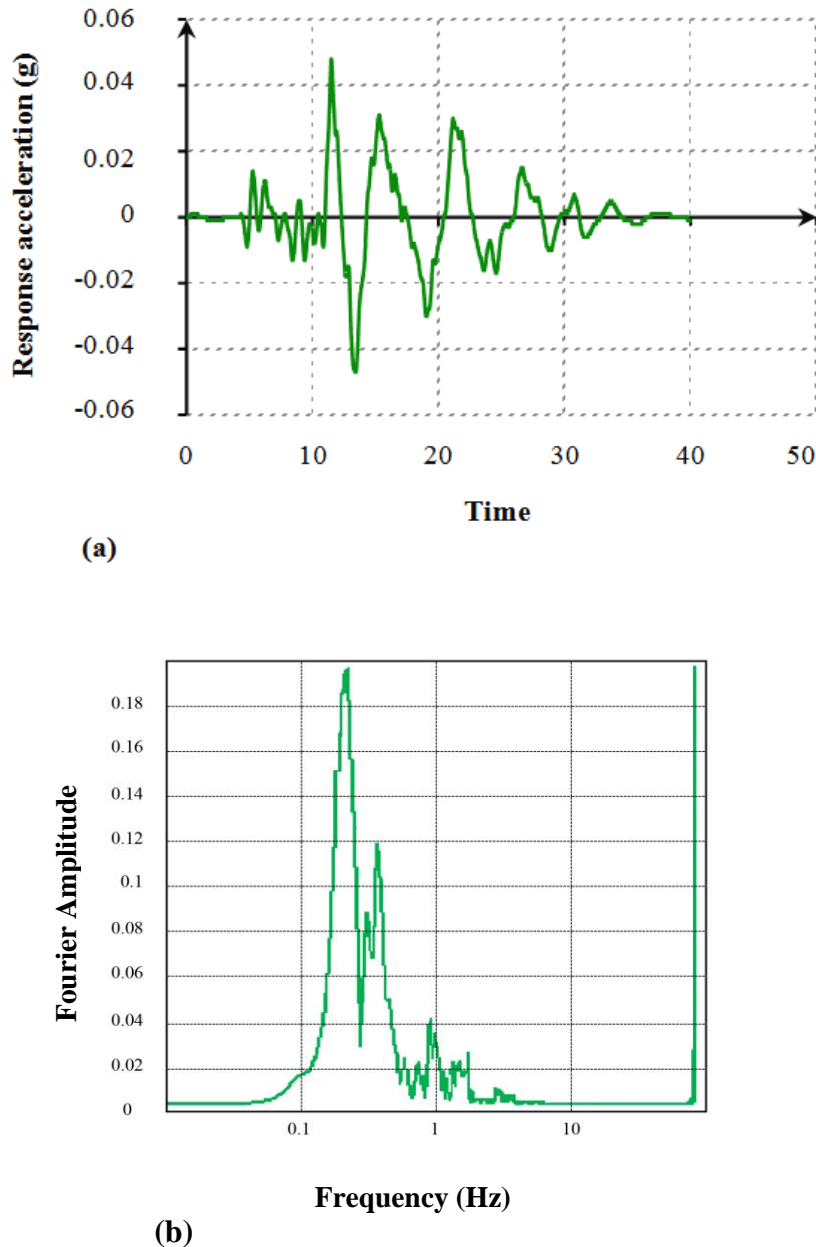
(a)

Frequency (Hz)

(b)

Fig. 8. (a) Response acceleration-time diagram of Landers earthquake (1992) and (b) corresponded time-frequency domain transformation

According to ASCE code [45], since maximum modal responses do not occur for different modes in an impact wave simultaneously, therefore, maximum modal responses in different members of a structure via a statistical method should be estimated. The mentioned statistical method should be as indicated by the maximum displacements of different modes and it should include the effects of probable interactions between different displacements close together that are derived from different modes. The peak value of the total response U is estimated by combining the peak modal response of individual modes using the modified double sum equation as given by Eq. (12) [46]:

(12)

$$F_i = \max\left[\left(\sum_{i=0}^{h/t} G(x_1)\right) + \left(\sum_{h/t}^{2h/t} G(x_2)\right) + \dots + \left(\sum_{(t-1)h/t}^{h} G(x_u)\right)\right]$$

$$where: \; G(x_u) = U^2 = \sum_{n=1}^{N} U_n^2 + 2\sum_{n=1}^{N-1} U_n^2 \sum_{m=n+1}^{N} \rho_{nm} U_n U_m$$

In Eq. (12), F_i is the fitness function, t is the section number, h is the maximum structure height, U_n is the maximum modal response in the nth mode, and ρ_{nm} is the modified correlation factor defined as:

$$\rho_{nm} = \alpha_n \alpha_m + \sqrt{((1-\alpha_n^2)(1-\alpha_m^2))}\, \rho_{nm} \qquad (13)$$

where α_n is the rigid response coefficient in the nth mode and ρ_{nm} is the correlation coefficient of the damped periodic part of modal responses, given by the well-known CQC rule. For damped periodic modes, $\alpha = 0$, and modified double sum equation reduces to CQC and for $\rho_{nm}=0$, modified double sum method reduces this to the SRSS. Equations (12) and (13) include the effect of rigid response of high frequency modes in the modified correlation coefficient ρ_{nm}. The rigid response coefficient α_n is defined as [47]:

$$\alpha_n = -\frac{\displaystyle\int_0^{t_d} \ddot{x}_n(t)\ddot{u}_g(t)dt}{t_d \sigma_n^{\ddot{x}} \sigma^{\ddot{u}_g}} \qquad (14)$$

where $\ddot{x}_n(t)$ is the acceleration response, $\sigma_n^{\ddot{x}}$ and $\sigma^{\ddot{u}_g}$ are the standard deviations of $\ddot{x}_n(t)$ and, $\ddot{u}_g(t)$, respectively, and t_d is the duration of responses. The modal responses, having a frequency less than rigid frequency, have a rigid content, and the value of α gradually reduces from 1 to zero from a key frequency f_2 to another key frequency f_1 [46]. The key frequency f_2 is the lowest frequency at which the rigid response coefficient becomes 1 and the key frequency f_1 is the highest frequency at which the rigid response coefficient becomes zero. An approximate equation for α_n can be represented by a straight line between the two key frequencies f_1 and f_2 on a semi logarithmic graph, which is given by Eq. (15) [46]:

$$\alpha_n = \frac{\ln\dfrac{f_n}{f_1}}{\ln\dfrac{f_2}{f_1}} \qquad 0 \leq \alpha_n \leq 1 \qquad (15)$$

where f_n is the modal frequency (Hz) and the key frequencies f_1 and f_2 can be expressed as,

$$f_1 = \frac{(S_A)_{\max}}{2\pi(S_V)_{\max}} \qquad (16)$$

$$f_2 = \frac{(f_1 + 2f^r)}{3} \qquad (17)$$

where $(S_A)_{max}$= maximum spectral acceleration, $(S_V)_{max}$ = maximum spectral velocity and f^r= rigid frequency.

In this study, the number of variables is equal to 6, and 18 constraints have been considered. The sections number is equal to seven. It implies that the height of the structure is 21.0 m, and therefore the length of each section is found to be 3.0 m. At the first, ρ_{nm} was calculated then the square of total response $G(x_u)$ was computed using ρ_{nm}, U_n and U_m parameters. Each of the variables should be less than the maximum modal response corresponding to that mode in the each section. Eq. (12) was employed as the fitness function in this framework. This function was maximized by the GA system in the process of evolutionary optimization. When performing the OSP method via the GA technique, certain parameters are required such as constraints, fitness function, population size, elite individuals, crossover method, crossover individuals, mutation individuals, and fitness value. Table 7 demonstrates the values of GA parameters. Figure 9 clearly shows the evolution process of best fitness values of GA according to TTFD method. Finally, after obtaining $G(x_u)$ values using the optimization process, the Lagrangian interpolation was undertaken in each section considering the initial results of the square of total response, due to finding the optimal locations in each section.

According to this optimization method and considering the GA results, the best sensor locations in the BI building are presented as the final results in Table 8-10.
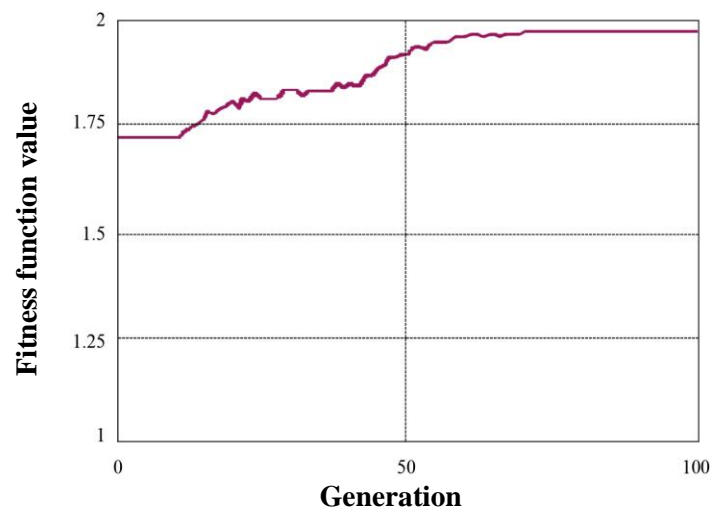
Fig. 9. The evolution progress of the best fitness value of GA according to TTFD method

Table 7. The values of GA parameters (TTFD)

Population	Elite individuals	Crossover individuals	Mutation individuals	Fitness value
100	39	50	32	1.98

Table 8. Details of OSP by GA in the seven sections using TTFD approach (Landers-1992)

Stage	1 (0-3.0 m)	2 (3.01-6.0 m)	3 (6.01-9.0 m)	4 (9.01-12.0 m)	5 (12.01-15.0 m)	6 (15.01-18.0 m)	7 (18.01-21.0 m)
X direction (m)	1.98	4.28	7.79	10.08	13.12	16.47	19.88
Y direction (m)	1.12	3.92	7.16	9.86	12.74	16.04	19.33
Z direction (m)	1.39	4.09	7.39	10.01	12.96	16.19	19.57

Table 9. Details of OSP by GA in the seven sections using TTFD approach (San Fernando-1971)

Stage	1 (0-3.0 m)	2 (3.01-6.0 m)	3 (6.01-9.0 m)	4 (9.01-12.0 m)	5 (12.01-15.0 m)	6 (15.01-18.0 m)	7 (18.01-21.0 m)
X direction (m)	1.54	3.76	7.31	9.73	12.86	15.95	19.47
Y direction (m)	0.96	3.57	6.92	9.29	12.43	15.71	18.92
Z direction (m)	1.21	3.63	7.17	9.58	12.64	15.83	19.28

Table 10. Details of OSP by GA in the seven sections using TTFD approach (Northridge-1994)

Stage	1 (0-3.0 m)	2 (3.01-6.0 m)	3 (6.01-9.0 m)	4 (9.01-12.0 m)	5 (12.01-15.0 m)	6 (15.01-18.0 m)	7 (18.01-21.0 m)

X direction (m)	1.76	3.97	7.46	9.87	12.94	16.12	19.51
Y direction (m)	1.04	3.69	7.01	9.42	12.52	15.85	19.08
Z direction (m)	1.28	3.86	7.22	9.78	12.81	15.96	19.34

8. Conclusion

In this paper, three reliable methods for OSP of a BI building, based on modal and NTA results have been utilized. Real-coded elitist GAs with uniform parent centric crossover operators and mutation operators were developed and used for the implementation of the OSP process.

Three different strategies, including MAC, EMAC, and TTFD were investigated for OSP in a 5-story BI building. The MAC algorithm is a basic OSP method whereas EMAC is a new algorithm containing the improved MAC and they utilize the free vibration analysis results on OSP process. In the following, a novel OSP approach was proposed by authors that was named TTFD algorithm. The mentioned approach uses NTA results as an exact seismic response; however, the MAC and EMAC algorithms utilize the modal analysis results. As a comparison, the OSP results revealed since the TTFD employs the accurate data (seismic response) as input, this led to acquiring the sensor locations with a high precision rate.

8. References

[1]. Wang, J., Lin, C., and Min Yen, S. (2007). A story damage index of seismically-excited buildings based on modal frequency and mode shape, *Engineering Structures*, 29(9), 2143-2157.

[2]. Allemang, R.J., and Brown, D.L. (1982). A correlation coefficient for modal vector analysis, In: *Proceedings of the international modal analysis conference*, 110-116, https://www.semanticscholar.org/paper/ A-Correlation-Coefficient-for-Modal-Vector-Analysis-Allemang-Brown/ 5b38c729b278f8af61491f6a643912c185 783cc8.

[3]. Ewins, D.J. (1984). *Modal testing: Theory and practice* (Dewey Number: 624.1/71), London: Research Studies Press Ltd.

[4]. Lieven, NAJ., and Ewins, DJ. (1988). Spatial correlation of mode shapes, the coordinate modal assurance criterion (COMAC), In: *Proceedings of the sixth international modal analysis conference*, vol. II, Hyatt, OR, Union College, 690-695.

[5]. Ndambi, J-M., Vantomme, J., and Harri, K. (2002). Damage assessment in reinforced concrete beams using eigenfrequencies and mode shapes derivatives, *Engineering Structures*, 24, 501-515.

[6]. Brasiliano, A., Doz, GN., and Brito, JLV. (2004). Damage identification in continuous beams and frame structures using the residual error method in the movement equation, *Nuclear Engineering and Design*, 227, 1-17.

[7]. Carne, T. G., and Dohrmann, C. R. (1994). A modal test design strategy for model correlation (Report Number: Conf-950240-4), In: *international modal analysis conference, Nashville,* TN, 927-933, http://adsabs.harvard.edu/abs/1995SPIE. 2460.927C.

[8]. Li, D. (2011). *Sensor placement methods and evaluation criteria in structural*

health monitoring, Ph. D. thesis, University of Siegen, Siegen.

[9]. Kammer, D.C. (1991). Sensor placement for on-orbit modal identification and correlation of large space structures, *Journal of Guidance, Control, and Dynamics (AIAA),* 14(2), 251-259.

[10]. Kammer, D.C. (1992). Effect of model error on sensor placement for on-orbit modal identification of large space structures, *Journal of Guidance, Control, and Dynamics (AIAA)*, 15 (2), 334-341.

[11]. Imamovic, N. (1998). *Validation of large structural dynamics models using modal test data*, Ph. D. thesis, Imperial College of Science, Technology & Medicine. London.

[12]. International, L. (1991). Large-scale modal testing of a space frame structure-from pretest analysis to FEA model validation, *Journal of Sound and Vibration*, 10, 6-16.

[13]. Heo, G., Wang, M.L., and Satpathi, D. (1997). Optimal transducer placement for health monitoring of long span bridge, *Soil Dynamics and Earthquake Engineering*, 16 (7-8), 495-502.

[14]. De Clack, L.P., and Avitabile, P. (1996). Development of several new tools for modal pre-test evaluation, In: *Proceedings of the 14th international modal analysis conference*, Dearborn, 1272-7, https://www.semanticscholar.org/paper/Development-of-Several-New-Tools-for-Modal-Pre-test-Declerck-Avitabile/23dafb143a8b709e1b84bd4def528b59cda0e0cb.

[15]. Kienay, D., Richrrrdson, M., and Blakely, K. (1989). Using finite element data to set up modal tests, *Journal of Sound and Vibration*, 23, 16-23.

[16]. Papadimitriou, C. (2004). Optimal sensor placement methodology for parametric identification for structural systems, *Journal of Sound and Vibration,* 278 (4), 923-947.

[17]. Papadimitriou, C. (2005). Pareto optimal sensor placement locations for structural identification, *Journal of Computer Methods in Applied Mechanics and Engineering,* 194 (12), 1655-1673.

[18]. Limongelli, M. P. (2003). Optimal location of sensors for reconstruction of seismic responses through spline function interpolation, *Journal of Earthquake Engineering Structure Dynamics*, 32, 1055-1074.

[19]. American Institute of Steel Construction (AISC) (2016), *in Manual of Steel Construction-Load Resistance Factor Design*, Chicago, AISC.

[20]. Ahmadi, S.L. and Tadjbakhsh, I.G. (1989). A comparative study of performances of various base isolation systems, Part 1: Shear beam structures, *Journal of Earthquake Engineering Structure Dynamics*, 18, 11-32.

[21]. Chen, C., Yeh, K., and Liu, F. (2009). Adaptive fuzzy sliding model control for seismically excited bridges with lead rubber bearing isolation, *International Journal of Uncertainty Fuzziness and Knowledge-Based Systems*, 17 (5), 705–727.

[22]. Lee-Glauser, G.J., Ahmadi, G., and Horta, L.G. (1997). Integrated passive/active vibration absorber for multistory buildings, *ASCE Journal of Structural Engineering*, 123, 499-504.

[23]. Su, L., Ahmadi, G., and Tadjbakhsh, I.G. (1989). Comparative study of base isolation systems, *ASCE Journal Engineering Mechanics*, 115, 1976-1992.

[24]. Robinson, W.H. (1982). Lead-rubber hysteretic bearings suitable for protecting structures during earthquakes, *Journal of Earthquake Engineering Structure Dynamics,* 10, 593-604.

[25]. Soong, T.T., and Spencer, B.F. (2002). Supplemental energy dissipation: State-of-the-art and state-of-the-practice, *Journal of Engineering Structures*, 24, 243-259.

[26]. Saiful islam, A.B.M., Rizwan hussain, R., jumaat, M., and Rahman, M.A. (2013). Nonlinear dynamically automated excursions for rubber-steel bearing isolation in multi-storey construction, *Journal of Automation in construction*, 30, 265-275.

[27]. Uniform Building Code (UBC) (1997). *International conference of building officials*, Whittier, CA: UBC.

[28]. Jangid, R.S., and Kelly, J.M. (2001). Base isolation for near-fault motions, *Journal of Earthquake Engineering Structure Dynamics*, 30, 691-707.

[29]. Rodriguez-Marek, A. (2000). *Near fault seismic site response*, Ph.D. Thesis, Civil Engineering, University of California, Berkeley, CA, USA.

[30]. Providakis, C.P. (2008). Effect of LRB isolators and supplemental viscous dampers on seismic isolated buildings under near-fault excitations, *Journal of Engineering Structures*, 30 (5), 1187-1198.

[31]. Baker, J.W. (2007). Quantitative classification of near-fault ground motions using wavelet analysis, *Bulletin of the Seismological Society of America*, 97, 1486-1501.

[32]. Mazza, F., and Vulcano, A. (2009). Nonlinear response of RC framed buildings with isolation and supplemental damping at the base subjected to near-fault earthquakes, *Journal of Earthquake Engineering*, 13, 690-715.

[33]. Mazza, F., Vulcano, A., and Mazza, M. (2012). Nonlinear dynamic response of RC buildings with different baseisolation systems subjected to horizontal and vertical components of near-fault ground motions, *The Open Construction and Building Technology Journal*, 6, 373-383.

[34]. Hu, J.W., and Leon, R.T. (2011). Analysis and evaluations for composite-moment frames with SMA PR-CFT connections, *Nonlinear Dynamics*, 65, 433-455.

[35]. Hu, J.W., Choi, E., and Leon, R.T. (2011). Design, analysis, and application of innovative composite PR connections between steel beams and CFT columns, *Smart Materials and Structures*, 20(2), 1-15.

[36]. Jangid, R.S. (2007). Optimum lead-rubber isolation bearings for near-fault motions, *Journal of Engineering Structures*, 29, 2503-2513.

[37]. Hu, J.W., Kang, Y.S., Choi, D.H., and Park, T. (2010). Seismic design, performance, and behavior of composite-Moment frames with steel beam-to-concrete filled tube column connections, *International Journal of Steel Structures*, 10, 177-191.

[38]. Hwang CL. and Yoon, K. (1981). Methods for Multiple Attribute Decision Making, *Multiple Attribute Decision Making*, 58-191.

[39]. Goldberg, D. E. (1989). *Genetic Algorithms in Search, optimization and machine learning*, Addison-Wesley Pub. Co., Reading, Mass., xiii, 412 pages.

[40]. Tongpadungrod, P., Rhys, T. D. L. and Brett, P. N. (2003). An approach to

optimise the critical sensor locations in one-dimensional novel distributive tactile surface to maximize performance, *Journal of Sensors and Actuators*, 105, 47-54.

[41]. Huang, W. P., Liu, J., and Li, H. J. (2005). Optimal sensor placement based on genetic algorithms, *Journal of Engineering Mechanics*, 22(1), 113-117.

[42]. Guo, H. Y., Zhang, L., Zhang, L. L. and Zhou, J. X. (2004). Optimal placement of sensors for structural health monitoring using improved genetic algorithms, *Journal of Smart Materials and Structures*, 13, 528-534.

[43]. Yi, T. H., Li, H. N. and Gu, M. (2011). Optimal sensor placement for health monitoring of high-rise structure based on genetic algorithm, *Journal of Mathematical Problems in Engineering*, 11.

[44]. Sadat Shokouhi, S.K., and Vosoughifar, H.R. (2013). Optimal sensor placement in the lightweight steel framing structures using the novel TTFD approach subjected to near-fault earthquakes, *Journal of Civil Structural Health Monitoring*, 3 (4), 257-267.

[45]. ASCE standard code (2005). *Minimum design loads for buildings and other structures*, ASCE, USA.

[46]. Gupta, A. K., Hassan, T. and Gupta, A. (1996). Correlation coefficients for modal response combination of non-classically damped systems, *Journal of Nuclear Engineering and Design*, 165, 67-80.

[47]. Dong, C. (1998). Generalized genetic algorithm, *Journal of Exploration of Nature*, 63(17), 33-37.